



Time-dependent permeability evolution in compacting volcanic fracture systems and implications for gas overpressure



Jamie I. Farquharson^{a,*}, Fabian B. Wadsworth^b, Michael J. Heap^a, Patrick Baud^a

^a Géophysique Expérimentale, Institut de Physique de Globe de Strasbourg (UMR 7516 CNRS, Université de Strasbourg/EOST), 5 rue René Descartes, Strasbourg cedex 67084, France

^b Earth and Environmental Sciences, Ludwig-Maximilians-Universität, Theresienstrasse 41, München, Germany

ARTICLE INFO

Article history:

Received in revised form 28 April 2017

Accepted 30 April 2017

Available online 3 May 2017

Keywords:

Tuffisite

Explosive eruptions

Outgassing

Pressurisation

Porosity

Sintering

ABSTRACT

Volcanic eruptions are driven by the ascent of volatile-laden magma. The capacity of a volcano system to outgas these volatiles—its permeability—controls the explosive potential, and fractures at volcanic conduit margins play a crucial role in tempering eruption explosivity by acting as outgassing pathways. However, these fractures are often filled with hot volcanic debris that welds and compacts over time, meaning that these permeable pathways have a finite lifetime. While numerous studies emphasize that permeability evolution is important for regulating pressure in shallow volcanic systems, how and when this occurs remains an outstanding question in volcanology. In this contribution, we show that different pressure evolution regimes can be expected across a range of silicic systems as a function of the width and distribution of fractures in the system, the timescales over which they can outgas (a function of depth and temperature), and the permeability of the host material. We define *outgassing*, *diffusive relaxation*, and *pressure increase* regimes, which are distinguished by comparing the characteristic timescales over which they operate. Moreover, we define a critical permeability threshold, which determines (in concert with characteristic timescales of diffusive mass exchange between the pore and melt phases) whether systems fracture and outgas efficiently, or if a volcano will be prone to pressure increases, incomplete healing, and explosive failure.

© 2017 Elsevier B.V. All rights reserved.

1. Introduction

The ability of a volcanic system to outgas, governed by the permeability of rock and magma, influences eruption explosivity (e.g. Woods and Koyaguchi, 1994). In particular, the generation of fractures is thought to be a key mechanism allowing the dissipation of magmatic gases—and hence, pressure—in volcanic environments (e.g. Gonnermann and Manga, 2003; Tuffen and Dingwell, 2005; Kolzenburg et al., 2012; Castro et al., 2014; Kendrick et al., 2016; Saubin et al., 2016). Indeed, recent laboratory studies (Nara et al., 2011; Farquharson et al., 2016a; Heap and Kennedy, 2016) highlight that fractures in volcanic rock can increase permeability by several orders of magnitude. Heap and Kennedy (2016) fractured samples of andesite in tension: a key finding is that—irrespective of their initial physical properties—samples exhibited approximately the same permeability once a through-running fracture had been imposed (see Fig. 1). Nevertheless, while the compiled permeability–porosity data in Fig. 1 indicate that the “fracture-limited” permeability of

these volcanic materials is typically on the order of 10^{-11} m², it is important to consider that these data represent laboratory-scale measurements of freshly fractured material. In nature, such fractures typically become infilled with angular fragments, juvenile or otherwise (e.g. Kolzenburg et al., 2012; Kendrick et al., 2016; Saubin et al., 2016). Moreover, under appropriate temperature and pressure conditions, these infilled fractures may heal over time due to progressive sintering of the interior material (e.g. Stasiuk et al., 1996; Tuffen et al., 2003; Kolzenburg et al., 2012; Okumura and Sasaki, 2014; Wadsworth et al., 2014; Wadsworth et al., 2016a).

Fig. 2 shows two examples of fractured volcanic material with various degrees of allochthonous and autochthonous fracture infill and healing. Fig. 2A shows a saw-cut of a dense obsidian bomb containing a tuffisite approximately 30 mm in width, ejected during the 2008 rhyolitic eruption of Chaitén (Chile) (see Saubin et al., 2016, for further details). The tuffisite is characterised by juvenile material interspersed by transported lithics. Subsidiary fractures are also visible in the same bomb. Fig. 2B shows a Scanning Electron Microscope (SEM) image of a sample of dense andesite from Volcán de Colima (see Farquharson et al., 2016b). In this case, the sample contains a throughgoing fracture containing juvenile fragments. The granular material within the fracture has partially sintered. Similar features

* Corresponding author.

E-mail address: farquharson@unistra.fr (J.I. Farquharson).

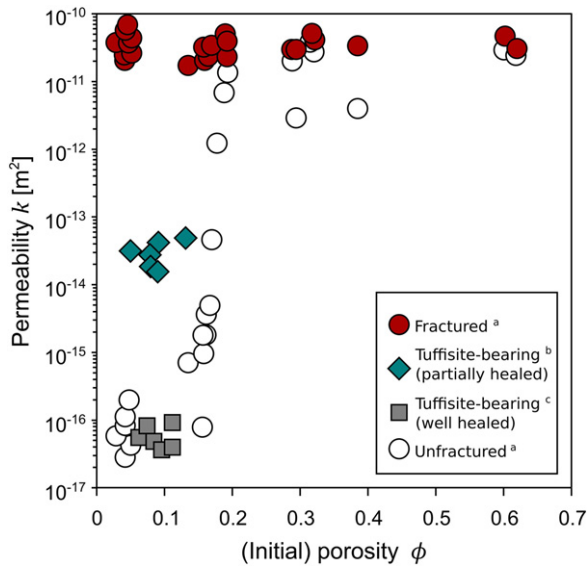


Fig. 1. Compiled permeability–porosity data illustrating the influence of fractures and fracture healing. Open circles represent initial unfractured permeability of andesite from [Heap and Kennedy \(2016\)](#). When fresh tensile fractures were imposed in the samples, permeability increased (filled circles). Samples of tuffisite-bearing andesite of comparable dimensions exhibited intermediate permeability relative to the fractured and unfractured material when sintering was incipient (diamonds), while the permeability of samples where sintering was more advanced (squares) are in line with the initial unfractured material. ^a[Heap and Kennedy \(2016\)](#); ^b[Farquharson et al. \(2016a\)](#); ^c[Kolzenburg et al. \(2012\)](#).

from Volcán de Colima are reported and described in [Kolzenburg et al. \(2012\)](#) and [Kendrick et al. \(2016\)](#).

Notably, the permeability of a fracture-bearing sample the andesitic block of [Fig. 2B](#) is two orders of magnitude greater than the (unfractured) host rock ($\sim 3 \times 10^{-14}$ compared to $\sim 2 \times 10^{-16}$ m² ([Farquharson et al., 2016b](#), see also [Fig. 1](#)). Nevertheless, this is approximately three orders of magnitude lower than the fractured andesites of [Fig. 1](#) ([Heap and Kennedy, 2016](#)). On the other hand, well-healed tuffisite-bearing material measured by [Kolzenburg et al. \(2012\)](#) exhibits permeabilities and porosities in line with the unfractured andesite of [Heap and Kennedy \(2016\)](#). This discrepancy on the laboratory scale indicates that a significant reduction in permeability can occur during fracture healing, fracture filling with granular material and with the progressive welding of the fracture fill. Thus, any in situ increase in permeability due to fracturing of volcanic material is likely transient if the fragments within the fracture can viscously sinter and compact over time (e.g. [Tuffen et al., 2003](#); [Wadsworth et al., 2014](#)), thereby reducing the permeability back to the pre-fractured state or indeed lower. This is in agreement with the findings of [Heap et al. \(2015\)](#), who performed permeability measurements on samples of natural variably-welded block-and-ash flow deposits.

Using available literature data, [Wadsworth et al. \(2016b\)](#) found that the permeability of granular volcanic materials—such as those that fill these fractures—scales with the porosity via the specific surface area of the evolving granular mixture. However, laboratory studies which constrain the permeability of variably-healed fractures, such as tuffisites, are few ([Kolzenburg et al., 2012](#); [Kendrick et al., 2016](#); [Farquharson et al., 2016b](#)); moreover, they are inherently concerned with permeability on relatively small scales ([Heap and Kennedy, 2016](#)), at a given point in time. Consequently, estimates for the equivalent permeability of fractured conduit margins and how this may change over time—crucial parameters for models of volcanic outgassing (e.g. [Jaupart, 1998](#); [Collinson and Neubeurg, 2012](#))—must be accomplished by incorporating these data into

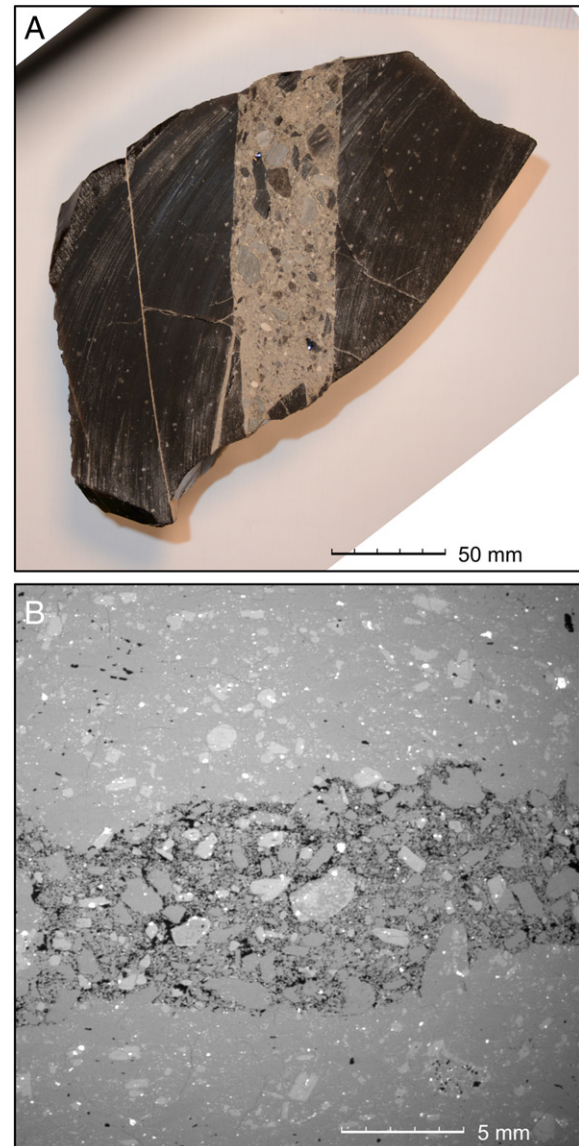


Fig. 2. Evidence of ash-filled fractures in volcanic environments. A) Sawn block of obsidian containing a large ~ 30 mm wide, through-going tuffisite, formed in the 2008 eruption of Volcán Chaitén, Chile ([Saubin et al., 2016](#)). B) Scanning Electron Microscope (SEM) image of fractured andesite collected at Volcán de Colima, Mexico. In the SEM image, porosity appears as black, whereas the groundmass and fracture-filling particles are in shades of gray. In both cases, the granular fracture-fill has partially sintered back together into a coherent material, providing snapshots of the healing process.

upscaling models which can evolve over time. A recent numerical modelling study by [Chevalier et al. \(2017\)](#) highlighted that the decrease of permeable gas loss at the conduit walls (i.e. the conduit–host rock edifice)—as a consequence of dome growth and loading of the edifice—can result in significant gas pressure increase within the conduit. Their study represents an important advance in our ability to couple physical mechanisms with the evolution of permeability and gas pressure in volcanic systems. Here, our contribution focusses on transient permeability increase resulting from near-conduit fracture generation, providing a detailed exploration of the capacity for lateral gas flow: a parameter often treated as a static boundary condition in complex two-dimensional gas evolution models.

By coupling experimentally-derived permeability reduction timescales ([Heap et al., 2015](#)) with a scaling for the distribution of

fluid flow in parallel layers (Heap and Kennedy, 2016; Farquharson et al., 2016b), the time-dependent equivalent permeability of a fractured volcanic conduit can be modelled. In this case, the equivalent permeability is that of the edifice rock or magma populated with fractures filled with granular juvenile debris. We present the constituent model parameters before applying the model to two case studies—Mount Unzen (Kyūshū, Japan) and Volcán Chaitén (Chile)—which form the basis of a discussion focussed on outgassing efficiency and pore-pressure build-up timescales. We predict the regime change from efficient outgassing to explosive eruption as gas pressure build-up competes with closing and healing of fractures by examining the timescales over which the governing mechanisms operate. This regime change defines whether or not a fractured system will be prone to pore pressure build-up as a consequence of sintering-driven compaction. We analyse literature-derived data pertaining to six different silicic volcanoes, highlighting that the potential for explosive failure of healing fractures differs from system to system. The MATLAB® program developed to tackle this problem is provided as Supplementary Material, and can be used to determine equivalent permeability for a range of user-defined scenarios, as well as number of ancillary properties such as pressure- and temperature-dependent magma and fluid viscosity.

2. An empirical porosity reduction model

Volcanic particles will densify viscously if the temperature T of the particles remains above their glass transition temperature T_g (e.g. Wadsworth et al., 2014). If we assume that the material properties of these particles are homogenous, then the following empirical compaction model (Russell and Quane, 2005) can be employed to cast the time-dependent porosity ϕ as a function of time t :

$$\phi(t) = \frac{\beta}{\beta - \alpha}; \beta = \ln \left[\frac{\alpha \sigma}{\eta_0 (1 - \phi_i)} t + \exp \left(\frac{-\alpha \phi_i}{1 - \phi_i} \right) \right] \quad (1)$$

where η_0 is the initial effective viscosity of the melt plus crystal cargo at zero porosity—that is, the viscosity of the particles—and ϕ_i is the initial porosity. σ is the external stress driving compaction in our model, which we assume to be the overlying lithostatic (or magmatic) stress, referred to hereafter as the vertical compaction stress σ_{zz} (e.g. McKenzie, 2011). The role of the dimensionless coefficient α is to scale the dependence of the effective viscosity of the densifying granular mixture on ϕ during compaction and therefore encompasses several unconstrained parameters such as the pore size and shape, particle size and shape, and pore and particle size distribution (e.g. Heap et al., 2015). We adopt a constant value of $\alpha = 2$, based on high-temperature (800–900 °C) compaction experiments performed by Heap et al. (2014) on crushed and sieved material originally derived from block-and-ash flow deposits at Mount Meager (Canada). The experimental material was of dacitic bulk composition (~68 wt % SiO₂) with a rhyolitic glass groundmass (~76 wt % SiO₂; see Stewart (2002)).

The initial porosity ϕ_i is taken as 0.40, which is typical for polydisperse granular material close to a random maximum packing (note that the equivalent for a monodisperse material would be higher). The vertical compaction stress is a function of depth \hat{z} taken as $\sigma_{zz} = \rho_b \cdot g \hat{z}$, where ρ_b and g are the bulk density of the overlying material and acceleration due to gravity, respectively.

The melt viscosity in Eq. (1) is a parameter that can vary by orders of magnitude in volcanic liquids or suspensions as a function of temperature, water content, and crystallinity. Herein, two cases are tackled: (1) for aphyric magmas where the pure liquid viscosity η replaces η_0 in Eq. (1) and (2) where η_0 is the viscosity of

a liquid suspending crystals. Both cases employ the model of Hess and Dingwell (1996) to describe the liquid viscosity as a function of temperature and the dissolved water concentration as follows:

$$\log_{10}(\eta) = a + \frac{b}{T-c}; \begin{cases} a = a_1 + a_2 \ln(C_{H_2O}) \\ b = b_1 + b_2 \ln(C_{H_2O}) \\ c = c_1 + c_2 \ln(C_{H_2O}) \end{cases} \quad (2)$$

for which T is in Kelvin and the parameters a , b , and c depend on the dissolved water content C_{H_2O} ($a_1 \dots c_2$ are given in Table 1 or in Hess and Dingwell (1996)). In our model, 10^{12} Pa·s is taken as a blunt description of η at T_g (e.g. Giordano et al., 2008), and we cast $\eta(T, C_{H_2O})$ as a function of the absolute depth of each fracture by assuming a homogeneous upper crustal density (dependent on the case study), and assuming that the magma is initially water-saturated. We note that compaction and fracture evolution is not necessarily precluded at temperatures below T_g (e.g. Farquharson et al., 2016a). Mechanical deformation of fractures at subsolidus temperatures (e.g. fault sliding, comminution, or rotation of rigid fragments) is not addressed in this contribution.

Equilibrium values of C_{H_2O} are determined using a temperature- and depth-dependent solubility model (Liu et al., 2005):

$$C_{eq} = \frac{s_1 p^{0.5} + s_2 p - s_3 p^{1.5}}{T} + s_4 p^{1.5} \quad (3)$$

where C_{eq} is the equilibrium solubility of H₂O in a rhyolitic melt at temperature T under pressure p (coefficients $s_1 \dots s_4$ are given in Table 1 or in Liu et al. (2005)). Assuming the crystals are suspended in the larger volcanic particles such that the viscosity of semi-crystalline particles can be taken as a suspension viscosity, the influence of crystal fraction Φ on the initial effective viscosity η_0 is given by the model of Maron and Pierce (1956) (see also Mueller et al., 2010) for suspensions of particles in viscous liquids:

$$\eta_0 = \eta \left(1 - \frac{\Phi}{\Phi_m} \right)^{-2} \quad (4)$$

where η is the melt viscosity as derived from Eqs. (2) and (3), and Φ_m is the maximum packing of crystals. Φ_m is dependent on the shape of the crystals which in turn depends on their aspect ratio r_p , described by Mueller et al. (2010) in the following form:

$$\Phi_m \simeq \Phi_m^* \exp \left[-\frac{\log_{10} r_p^2}{2\gamma^2} \right] \quad (5)$$

where Φ_m^* is the maximum packing fraction when $r_p = 1$ (calibrated as 0.656), and γ is an empirical parameter calibrated by Mueller et al. (2011) to be 1.08 (for their data: experimental results for crystal-bearing magma analogues). We highlight that although the Maron–Pierce equation has not—to the authors' knowledge—been verified experimentally for the compaction of fragmented magma, a study by Müller et al. (2007) found that the viscosity of sintering glass powders was well described in the form of Eq. (4).

3. Extension to a permeability reduction model

Porosity ϕ and permeability k of volcanic materials are often related using one or more power laws (e.g. Klug and Cashman, 1996; Mueller et al., 2005; Farquharson et al., 2015a; Kushnir et al., 2016; Heap and Kennedy, 2016; Wadsworth et al., 2016b). Herein, we employ a two-slope relation, valid for the evolution of permeability

Table 1
Notation used.

Symbol	Meaning	Units	Value	Reference
a	Characteristic particle radius	m	–	Eq. (16)
a	Limit viscosity at infinite temperature	Pa · s	–	Eq. (2)
a_1	Viscosity coefficient	–	3.545	Hess and Dingwell (1996)
a_2	Viscosity coefficient	–	0.833	Hess and Dingwell (1996)
b	Pseudo-activation energy	J mol ⁻¹	–	Eq. (2)
b_1	Viscosity coefficient	–	9601	Hess and Dingwell (1996)
b_2	Viscosity coefficient	–	2368	Hess and Dingwell (1996)
c	Vogel–Fulcher–Tammann Temperature	°C; K	–	Eq. (2)
c_1	Viscosity coefficient	–	195.7	Hess and Dingwell (1996)
c_2	Viscosity coefficient	–	32.25	Hess and Dingwell (1996)
e	Compaction timescale factor	–	–	–
f	Helmholtz free energy	–	–	Appendix A
f	Dimensionless Helmholtz free energy	–	–	Appendix A
g	Acceleration due to gravity	m s ⁻²	9.806	–
g	Dimensionless Gibbs energy	–	–	Appendix A
h	Enthalpy	kJ kg ⁻¹	–	Appendix A
h_x	Enthalpy in region x	–	–	–
h^*	Reference enthalpy	kJ kg ⁻¹	–	Appendix A
h	Dimensionless enthalpy	–	–	Appendix A
i	Serial number	–	–	Appendix A
j	Serial number	–	–	Appendix A
k	Permeability	m ²	–	Eq. (6)
k_0	Initial permeability	m ²	–	–
k_{cr}	Critical permeability threshold	m ²	–	Eq. (19)
k_{fj}	Permeability of fracture j	m ²	–	–
k_{eq}	Equivalent permeability	m ²	–	Eq. (7)
ℓ	Total considered lengthscale	m	–	–
ℓ_C	Compaction lengthscale	m	–	Eq. (8)
n_f	Number of fractures	–	–	–
n_i	Pore fluid viscosity parameters	–	–	Appendix A
p	Pressure	MPa	–	–
$p_b - p_a$	Pressure drop over L	Pa	–	Eq. (12)
∇p	Driving pressure gradient	Pa	–	Eq. (13)
p_{fj}	Pressure within fracture j	Pa	–	–
p^*	Reference pressure	Pa	–	Appendix A
q	Fluid flux	m s ⁻¹	–	Eq. (13)
r	Residual component	–	–	Appendix A
r_p	Particle aspect ratio	–	1	Mueller et al. (2010)
s_1	Solubility law constant	–	354.94	Liu et al. (2005)
s_2	Solubility law constant	–	9.623	Liu et al. (2005)
s_3	Solubility law constant	–	1.5223	Liu et al. (2005)
s_4	Solubility law constant	–	0.00124	Liu et al. (2005)
t	Time	s	–	–
t_0	Start time	s	0	–
v	Pore fluid volume	m ³	–	–
w_{fj}	Width of fracture j	m	–	–
w_i	Width of intact material	m	–	Eq. (7)
x^*	Porosity changepoint	–	0.155	Heap et al. (2015)
\hat{z}	Depth (vertical unit vector)	m	–	–
\mathcal{A}	Cross-sectional area	m ²	–	Eq. (12)
A	Permeability–porosity prefactor	–	1.34×10^{-16}	Heap et al. (2015)
B	Permeability–porosity exponent	–	1.01	Heap et al. (2015)
C	Permeability–porosity prefactor	–	7.98×10^{-26}	Heap et al. (2015)
D	Permeability–porosity exponent	–	8.76	Heap et al. (2015)
B_{23}	Boundary of regions 2 and 3	MPa; K	–	Appendix A
B_{3a3b}	Boundary of regions 3a and 3b	–	–	Appendix A
C_{H_2O}	H ₂ O content	wt%	–	Eq. (3)
C_0	Reference H ₂ O content	wt%	1	Zhang et al. (1991)
C_{eq}	Equilibrium H ₂ O content	wt%	–	Eq. (3)
\mathcal{D}	Diffusivity coefficient	m ² s ⁻¹	–	Zhang et al. (1991)
Da_C	Compaction Darcy number	–	–	Eq. (17)
G	Specific Gibbs free energy	–	–	Appendix A
H	Fluid viscosity coefficient(s)	–	–	Appendix A
I	Fluid density coefficient(s)	–	–	Appendix A
J	Fluid density coefficient(s)	–	–	Appendix A
L	Lengthscale of permeability measurement	m	–	Eq. (12)
M	Saturation pressure parameter	–	–	Appendix A
N	Saturation pressure parameter	–	–	Appendix A
O	Saturation pressure parameter	–	–	Appendix A
Pe_C	Compaction Péclet number	–	–	Eq. (18)
Q	Fluid discharge rate	m ³ s ⁻¹	–	–
R	Specific gas constant of water	kJ kg ⁻¹ K ⁻¹	0.461526	Appendix A
T	Temperature	°C; K	–	–
T^*	Reference temperature	°C; K	–	Appendix A
T_g	Glass transition temperature	°C; K	–	–

Table 1

Symbol	Meaning	Units	Value	Reference
α	Rheological constant	–	2	Heap et al. (2014)
β	Compaction model parameter	–	–	Eq. (1)
γ	Particle shape parameter	–	1.08	Mueller et al. (2010)
δ	Fracture width ratio	–	–	Eq. (10)
η	Melt viscosity	Pa·s	–	Eq. (2)
η_0	Initial effective viscosity	Pa·s	–	Eq. (4)
θ	Dimensionless temperature	–	–	Appendix A
ϑ	Saturation pressure parameter	–	–	Appendix A
λ_C	Compaction timescale	s	–	Eq. (11)
λ_{Da}	Darcy outgassing timescale	s	–	Eq. (14)
$\lambda_{\mathcal{D}}$	Timescale for molecular diffusion of H ₂ O	s	–	Eq. (16)
ρ	Fluid density	kg m ⁻³	–	–
ρ^*	Reference fluid density	kg m ⁻³	–	Appendix A
ρ_b	Bulk density	kg m ⁻³	–	–
$\Delta\rho$	Fluid–bulk density contrast	kg m ⁻³	–	–
ϱ	Dimensionless fluid density	–	–	–
σ_{zz}	Vertical compaction stress (lithostatic or magmastic stress)	MPa	–	–
τ	Reciprocal dimensionless temperature	–	–	Appendix A
μ	Pore fluid viscosity	Pa·s	–	Eq. (9)
μ_0	Viscosity in the dilute-gas limit	–	–	Appendix A
μ_1	Viscosity due to finite density	–	–	Appendix A
μ_2	Critical enhancement of viscosity	–	1	Appendix A
μ^*	Reference pore fluid viscosity	Pa·s	1.00×10^{-6}	Appendix A
π	Dimensionless pressure	–	–	Appendix A
o	Ideal Gas component	–	–	–
ϕ	Porosity	–	–	–
ϕ_i	Initial porosity	–	0.40	–
ω	Dimensionless pore volume	–	–	Appendix A
ω_x	Dimensionless pore volume in region x	–	–	Appendix A
Φ	Crystal fraction	–	–	–
Φ_m	Maximum packing fraction of crystals	–	–	Eq. (5)
Φ_m^*	Reference packing fraction	–	0.656	Mueller et al. (2010)
Ω	Dimensionless fluid viscosity	–	–	Eq. (9)

at different stages of sintering-driven compaction of polydisperse volcanic particles (Heap et al., 2015):

$$k = \begin{cases} A\phi^B & \forall \phi \geq x^* \\ C\phi^D & \forall \phi < x^* \end{cases} \quad (6)$$

Experimentally determined values for A...D are given in Table 1 or in Heap et al. (2015). A threshold porosity value x^* is defined at $\phi = 0.155$, whereat the $k = f(\phi)$ relationship shifts from one power law trend to the other. Eq. (6) is used in concert with the porosity-reduction timescale (Eq. (1)) to give a timescale of permeability reduction during sintering-driven compaction of polydisperse materials. While permeability–porosity data for variably-compacted natural volcanic material are currently scarce, we note that the trend determined by Heap et al. (2015)—Eq. (6)—is generally in line with that determined through experimental compaction of rhyolitic melt over a broad range of porosities (e.g. Okumura and Sasaki, 2014).

To determine the equivalent permeability k_{eq} of the considered length of the conduit, we scale for a geometry whereby the fracture permeability occurs in discrete layers and the inter-fracture spaces are occupied by a host rock of lower permeability. This scaling uses the fracture widths relative to the total system length considered and has the form:

$$k_{eq} = \frac{k_0 w_i + \sum_{j=1}^{n_f} (w_{f_j} k_{f_j})}{\ell}; \quad w_i = \ell - \sum_{j=1}^{n_f} w_{f_j} \quad (7)$$

where k_0 is the host permeability (i.e. of the rock between the fractures), and ℓ is the total considered lengthscale (i.e. the length of the conduit, or a fracture “window”). Each fracture has a width w_f and permeability k_f , each successive $w_{f_j} k_{f_j}$ term representing the width and time-dependent permeability of each fracture up to n_f , the total number of fractures. The subscript j denotes the fracture number

from 1... n_f . (Note that the time-dependence of k_f stems from the time-dependent reduction in porosity as a function of the driving stress—Eq. (1)—related to permeability through Eq. (6).) The intact width w_i is given by the considered lengthscale minus the sum of all fracture widths. Fig. 3 provides a schematic illustration of this model setup. The theoretical system comprises a conduit adjacent to host rock with a given permeability k_0 (Fig. 3A). The distance EF corresponds to ℓ , the total considered length of the interface between the conduit and the edifice. In the first scenario (Fig. 3A), lateral migration of volatiles from the conduit is limited by k_0 . In the second scenario (Fig. 3B), lateral volatile movement is a function of the host rock permeability k_0 and permeabilities of fractures 1, 2, and 3 (i.e. k_{f_j} , where $j = 1, 2, \text{ and } 3$, respectively). Similarly, each of the fractures comprises a fracture width w_{f_j} . Fig. 3C illustrates the time-dependent reduction in fracture porosity (and in turn, permeability) as sintering-driven compaction progresses. Under a constant driving stress, k_{f_j} will tend towards k_0 . Fig. 3 shows how the width and permeability of each individual fracture contributes to the total fracture width (as in Eq. (7)). Note that this geometry is consistent with recent experimental data, which indicate that fractures in a (vertically) shearing magma column are likely to propagate preferentially in the horizontal plane (e.g. Kushnir et al., 2017). Vertical fractures would not contribute to the evolution of the permeability of the interface between the conduit and the host rock.

4. First order scaling of physical regimes

4.1. Assessing the calibrated range of the sintering model

Eq. (1) (Russell and Quane, 2005) assumes that the pressure driving compaction is constant across the width of the fracture from bottom to top. However, if a compacting fracture exceeds a threshold width, a significant spatial gradient in stress—and in turn, porosity—may develop between the edge and the fracture centre, in which

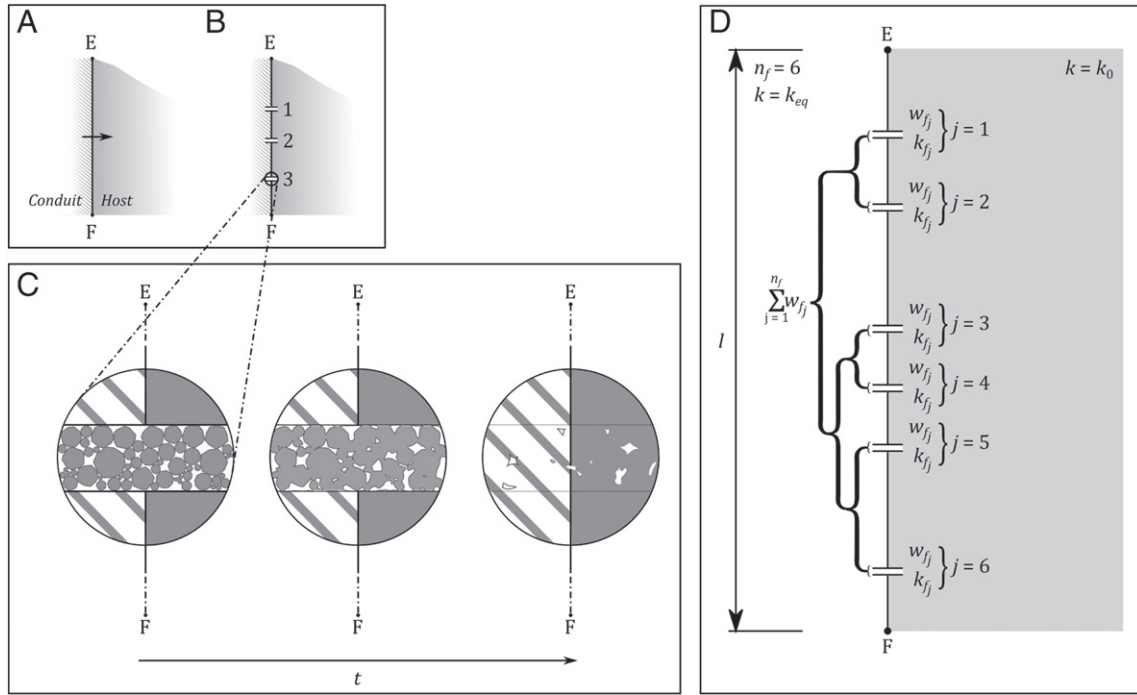


Fig. 3. Illustration of model geometry. In A) the lateral movement of fluids from the conduit to the host rock (i.e. outgassing) is shown by the arrow. The capacity for fluid migration is a direct function of the permeability of the interface EF , which has an initial value k_0 . In B) the permeability of the interface EF is now a function of the initial permeability k_0 and the permeability of each of the fractures 1, 2, and 3. In C), the time-dependent reduction in porosity of a fracture (as a consequence of sintering-driven compaction) is illustrated, which in turn yields a decrease in fracture permeability k_f over time t until the fracture heals. Finally, D) shows the geometry of the model. In this simplified case, there are six fractures along the length l ($n_f = 6$). The total width of the fractures is the sum of their individual widths (i.e. $\sum_{j=1}^{n_f} w_{f_j}$). Permeability of the interface EF is the equivalent permeability k_{eq} , a function of the intact material and fracture properties as given in Eq. (7).

case the kinetics of sintering-driven compaction would become more complex than encompassed by Eq. (1). To assess this explicitly, the compaction length ℓ_c can be calculated (see McKenzie, 1984), describing the length over which we can expect a significant spatial gradient in porosity to occur during compaction (Kennedy et al., 2016):

$$\ell_c = \left[k_{f_j} \left(\frac{\eta}{\mu} \right) \right]^{\frac{1}{2}} \quad (8)$$

where μ is the pore-fluid viscosity and η is the melt viscosity as previously defined. The most abundant magmatic fluid phase in shallow silicic conduits is H_2O (e.g. Holloway, 1981); accordingly, we assume the interstitial pore fluid is water vapour, which is both temperature- and pressure-dependent. Normalised fluid viscosity Ω is described here by the following simplified relation:

$$\Omega = \frac{\mu}{\mu^*} = \underbrace{\left[\frac{100\sqrt{\theta}}{\sum_{i=0}^3 \frac{H_i}{\theta^i}} \right]}_{\mu_0} \times \underbrace{\left[\varrho \sum_{i=0}^5 \left(\frac{1}{\theta} - 1 \right)^i \sum_{j=0}^6 H_{i,j} (\varrho - 1)^j \right]}_{\mu_1} \times \underbrace{\left[1 \right]}_{\mu_2} \quad (9)$$

where μ^* is a reference value of fluid viscosity, and θ and ϱ are dimensionless temperature and dimensionless fluid density, normalised to reference values T^* and ρ^* respectively. An explanation and the derivation of factors μ_0 , μ_1 , and μ_2 , including tables of values for coefficients i and j are given in Appendix A. In turn, the pressure- and temperature-dependent pore fluid viscosity is given by $\mu(p, T) = \Omega \cdot \mu^*$. The parameter δ is used here to define the ratio between the fracture width and compaction lengthscale (Eq. (8)), in order

to determine the fracture width range over which the compaction model may be assumed to be valid:

$$\delta = \frac{w_{f_j}}{\left[k_{f_j} \left(\frac{\eta}{\mu} \right) \right]^{\frac{1}{2}}} \quad (10)$$

Eq. (1) is here assumed to be valid while the fracture is sufficiently narrow ($\delta \ll 1$). If $\delta > 1$, then gradients of porosity will occur on the scale of the fracture width, meaning that the relatively simple kinetic model of Eq. (1) would no longer capture the complexities of sintering-driven compaction: in this case the scaling of permeability would be accordingly nontrivial (note however, that sintering-driven compaction is not necessarily precluded when $\delta > 1$; rather δ gives a realistic indication of the lengthscale over which compaction can be considered homogeneous). We impose a first order bound on δ of 10^0 (i.e. unity, also imposed in the accompanying MATLAB® model), above which Eq. (1) may not wholly capture the complexities of sintering wide fractures. It is reliant not only on the fracture width—wider fractures are more likely to exceed the critical width—but also the parameters which affect the viscosities of either the melt or the pore fluid (T, C_{H_2O}, Φ).

4.2. Gas escape versus gas retention

Consider an isothermal fracture, filled with some combination of particles and interstitial pore fluid. A given volume v of pore fluid will reside in the initial pore space, at an initial pressure p related to the volume by Boyle's law ($p \propto v^{-1}$). If a load is imposed perpendicular to the fracture plane, viscous compaction can occur as discussed above, and three ensuing scenarios may be envisaged. In the first instance, the rate of fluid flow from the fracture is larger than the rate of porosity reduction, in which case pressure remains in

equilibrium with the interstitial pore volume. We term this case the outgassing regime. If, on the other hand, pore pressure equilibrium cannot be maintained during compaction because the rate of Darcian fluid flow is lower than the rate at which a significant amount of compaction can occur (which is to say that the fluid flow timescale is greater than the compaction timescale), then two different possibilities arise. Volatiles may be exchanged with the sintering melt: the diffusive relaxation regime, or pore pressure may increase in accordance with Boyle's law as the volume of pore space is reduced: the pressure increase regime. Pressure increase can be a major driver of explosive fragmentation (e.g. Papale, 1999; Spieler et al., 2004; Melnik et al., 2005), so finding the conditions under which this regime is reached is of key importance.

Distinguishing which of these regimes dominates in a sintering fracture system depends on comparing the characteristic timescales (λ) over which they are operative. Accordingly, the following section develops a critical compaction time for pore pressure equilibrium (i.e. whether a given fracture is in the outgassing regime or otherwise). The compaction time is defined as the time taken for the porosity ϕ of a magma with initial effective viscosity η_0 to decrease by a factor of ϵ (an arbitrary small quantity) from the initial value ϕ_i . This is a function of the driving stress (e.g. Sparks et al., 1999; Nguyen et al., 2014); thus, from Eq. (1), the characteristic compaction timescale λ_C scales as:

$$\lambda_C \simeq \frac{\eta}{\alpha \sigma_{zz}}. \quad (11)$$

Darcy's law defines a proportional relationship between discharge rate Q of a fluid with viscosity μ through a porous medium, such that

$$Q = \frac{-kA}{\mu} \frac{p_b - p_a}{L} \quad (12)$$

where k is the permeability of the porous medium and A is the cross-sectional area for fluid flow. In a fluid transport system, flow is driven towards the region of lowest potential energy: in the special case of horizontal flow, this may be described by a differential between a region of relatively high pressure p_b to one of relatively lower pressure p_a (a pressure differential or pressure drop ∇p). L is thus defined as the lengthscale over which the pressure drop $p_b - p_a$ is occurring.

In more general notation, we can formulate Eq. (12) in terms of the flux q (i.e. the discharge per unit area) by dividing both sides of the equation by A :

$$q = \frac{-k}{\mu} \frac{\nabla p}{L}. \quad (13)$$

As q is in units of $m \ s^{-1}$, we can rearrange further to obtain a Darcy timescale in s (here called the outgassing time λ_{Da}) that describes the time it would take an aliquot of fluid to travel the length of the system and escape under a pressure gradient ∇p . Thus:

$$\lambda_{Da} = \frac{\mu L^2}{-k \nabla p}. \quad (14)$$

In the context of our model, the permeability k is that of each fracture k_{f_j} , and the system length L corresponds to the vertical distance from each fracture to its edge ($w_{f_j}/2$: see Fig. 3). Fluid flow through a given fracture (i.e. laterally) will be greater than vertical fluid flow from the fracture, making the latter orientation the limiting factor for gas escape. The initial pore pressure distribution with a dense bed of fluidised particles should approach the lithostatic pressure (e.g. Wilson, 1984; Miller, 1990; Sparks et al., 1999). As such, the initial pressure differential ∇p of the interstitial pore fluid is given by

$\Delta \rho \cdot g \hat{z}$, where $\Delta \rho$ represents the contrast between the bulk density of the granular sintering material and that of the pore fluid which—in concert with gravity and depth as defined previously—provides the driving force for Darcian outgassing from compacting fractures. The pressure differential is described by $\nabla p = (\rho_b - \rho) \cdot g \hat{z}$ or, equivalently, $\nabla p = \sigma_{zz} - \rho$. Given that pore fluid density ρ is negligible compared to that of the granular melt (i.e. $\rho \ll \rho_b$: see Appendix A), it can be discounted and thus ∇p becomes equivalent to σ_{zz} :

$$\lambda_{Da} = \frac{\mu \cdot \left(\frac{w_{f_j}}{2}\right)^2}{k_{f_j} \sigma_{zz}}. \quad (15)$$

A third timescale to consider is that of volatile resorption from the interstitial pore space into the sintering particles (i.e. the timescale for molecular diffusion of water). This timescale λ_D is obtained by considering that the timescale of diffusive resorption is controlled by total surface area of the particles (e.g. Sparks et al., 1999), and can be estimated by:

$$\lambda_D = \frac{a^2}{D} \quad (16)$$

where a is the characteristic particle radius and D is the diffusivity coefficient of the melt.

Comparing the timescales of compaction (Eq. (11)) and outgassing (Eq. (15)), defines a dimensionless compaction Darcy number Da_C (describing the competition between the effects of medium permeability, characteristic lengthscale, and viscous compaction):

$$Da_C = \frac{\lambda_C}{\lambda_{Da}} = \frac{\eta k_{f_j}}{\alpha \mu \cdot \left(\frac{w_{f_j}}{2}\right)^2}. \quad (17)$$

$Da_C > 1$ implies that the pore pressure can equilibrate during compaction such that no pore pressure increase is expected and the system is in the *outgassing* regime. By contrast, for $Da_C < 1$, the system may be in either of the *pressure increase* or *diffusive relaxation* regimes as compaction proceeds. The ratio of the compaction timescale and the characteristic diffusion timescale yields a compaction Péclet number Pe_C (the ratio of compaction and diffusive processes during compaction), such that:

$$Pe_C = \frac{\lambda_C}{\lambda_D} = \frac{\eta D}{\alpha \sigma_{zz} \cdot a^2}. \quad (18)$$

$Pe_C > 1$ indicates that molecular diffusion of water can proceed at a pace sufficiently rapid to compensate for the ongoing reduction in porosity. The system is thus in the *diffusive relaxation* regime, and stress is dissipated diffusively through volatile resorption. On the other hand, if $Pe_C < 1$, then reduction of the pore space occurs at a faster rate than can be compensated by Darcian or diffusive processes. As such, the interstitial pore pressure will increase in accordance with Boyle's law (i.e. $w_{f_j} \phi^{-1} \propto p_{f_j}$, where p_{f_j} is the pore pressure within fracture j).

Thus we have three conditions:

1. $\lambda_{Da} < \lambda_C$, the *outgassing* regime,
2. $\lambda_{Da} > \lambda_C > \lambda_D$, the *diffusive relaxation* regime, and
3. $\lambda_{Da} > \lambda_D > \lambda_C$, the *pore pressure increase* regime

Following this line of reasoning indicates that a critical permeability exists—which will be hereafter termed k_{cr} —which represents the minimum permeability that will allow pore fluid to migrate and

outgas from a fracture (i.e. by rearranging for the case of $\lambda_C = \lambda_D$ such that $Da_C = 1$):

$$k_{cr} = \frac{\alpha\mu \cdot \left(\frac{w_{fj}}{2}\right)^2}{\eta} \quad (19)$$

Significantly, defining this threshold offers a quantitative foundation upon which to base discussion on the propensity for pore pressure to evolve in volcanic fracture systems. Fig. 4 plots k_{cr} against the ratio of melt and pore fluid viscosities, contoured for different fracture widths. If fracture permeability is equal to or less than the critical permeability—for given melt and pore fluid viscosities—interstitial pore pressure may increase (dependant on Eq. (17)), precluding effective sintering of the fracture and pressurising the system, perhaps towards failure. Given the high permeability of a newly generated fracture (Heap and Kennedy, 2016), the requisite fracture width to allow $k_{fj} = k_{cr}$ is impossibly large for relevant viscosities (on the order of hundreds or thousands of m). However, as sintering-driven permeability reduction occurs, Da_C will tend towards unity and k_{fj} will tend towards k_{cr} . Assuming that the fractured material will always tend to sinter back towards its pre-fracture state (reasonable for low-crystallinity systems), then pore pressure build-up is always precluded in cases where the initial host permeability k_0 is below k_{cr} .

Whether or not pore pressure will ultimately increase depends also on the diffusion timescale λ_D (Eq. (16)). Calculation of this timescale requires the characteristic particle size within the healing fracture to be known. This may be evaluated from preserved ejecta or dissected conduits: for example, Saubin et al. (2016) note a particle size of $\sim 60 \mu\text{m}$ or greater (i.e. $a = 3.0 \times 10^{-5} \text{ m}$) for the tuffsite of Fig. 2A. Through a series of dehydration experiments on

hydrous rhyolitic melts, (Zhang et al., 1991; Zhang, 1999) correlate \mathcal{D} to temperature and water content such that

$$\mathcal{D}(\text{H}_2\text{O}) = \frac{C_{\text{H}_2\text{O}}}{C_0} \exp\left(-16.83 - \frac{10992}{T}\right) \quad (20)$$

where $C_{\text{H}_2\text{O}}$ and C_0 are the water content and a reference value (1 wt %), respectively, and T is in Kelvin. For the temperature range considered in our model, values of \mathcal{D} tend to be on the order $10^{-12} \text{ m}^2 \text{ s}^{-1}$ (in agreement with other experimentally-derived empirical approximations of \mathcal{D} , e.g. Doremus, 2000; Okumura and Nakashima, 2004). Accordingly, we obtain typical values for λ_D on the order of s to min. Note that more complex models for water diffusivity in magmatic liquids have since been proposed, including Zhang and Behrens (2000), Ni and Zhang (2008), and Zhang and Ni (2010). These more recent models seek to refine the pressure-dependence of $\mathcal{D}(\text{H}_2\text{O})$, which is not considered here.

Pressure evolution in sintering fractures can be determined by constraining the dimensionless ratios Da_C and Pe_C (Eqs. (17) and (18)). The former relates to the evolution of the permeability of an individual fracture relative to the critical threshold for that fracture (k_{fj} and k_{cr}), while the latter delimits the relative timescales of diffusive mass transport and fracture healing. We highlight that in either case, these relations rely on fracture depth (i.e. pressure): the compaction Darcy number is governed partially by $\mu(p)$, while the compaction Péclet number is governed $\mathcal{D}(\text{H}_2\text{O})$, in turn a function of $C_{eq}(p)$. Note that in the first case, the pressure-dependent variable is part of the denominator, while for Pe_C , the pressure-dependent variable comprises part of the numerator. Ultimately, this means that deeper fractures will exhibit relatively high values of k_{cr} and short λ_D times, whereas shallow fractures will have lower values of k_{cr} and longer λ_D times (all other factors being equal). Thus in general, shallow fracture systems are more likely to outgas volatiles via Darcian flow than deep fracture systems. However, in the case where the host permeability is lower than the critical threshold, deep fracture systems may be relatively more likely to dissipate stress by way of efficient mass diffusion, whereas pressure increase may be anticipated in the shallow case.

4.3. A critical permeability threshold in natural systems

In concert with constraint of the typical fracture widths observed in a given system, estimates of pre-eruptive $\eta_0(T, C_{\text{H}_2\text{O}}, \Phi)$ and $\mu(p, T)$ can be used to determine the critical permeability threshold for that system. Fig. 4 shows ranges of k_{cr} for six different volcanic systems, where the relevant data are available in the literature or can be modelled using the equations above (Eqs. (2)–(5), (9)).

- At Puyehue–Cordón Caulle (Chile, Schipper et al. (2013) provide estimates of mm- to m-scale fractures in rhyolite. Despite relatively high post-emplacement crystallinities (e.g. Schipper et al., 2013) and hence high post-emplacement viscosities (e.g. Farquharson et al., 2015b), the Puyehue–Cordón Caulle magma was estimated to be aphyric in the magma chamber and close to aphyric on eruption, with phenocrysts embodying approximately 5% by volume (Castro et al., 2013). The storage temperature has been estimated between 870 and 920 °C. Repetitive fracture and healing and ephemeral gas venting has been proposed to occur at relatively shallow depth in the Puyehue–Cordón Caulle system (Schipper et al., 2013). Thus we impose equilibrium water contents corresponding to 200–20 m depth: the inferred range for shallow sub-surface magma migration at Puyehue–Cordón Caulle (Castro et al., 2016). Calculated viscosities are therefore somewhat higher (η_0 on the order of 10^6 – $10^8 \text{ Pa}\cdot\text{s}$) than those estimated for the storage conditions by Castro et al. (2013).

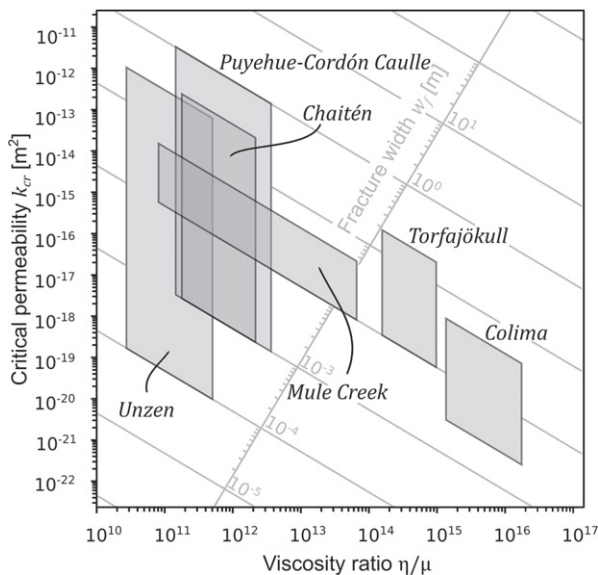


Fig. 4. Dimensional analysis. The critical permeability k_{cr} (Eq. (14)) is shown versus the viscosity ratio η/μ for different fracture widths w_{fj} . When a fracture is generated, its permeability will be high. This permeability decreases with time as a consequence of sintering-driven compaction. If, for a given w_{fj} and a given η/μ , the permeability of the fracture k_{fj} intersects the critical permeability, then pore pressure will be in disequilibrium. Thus, if the pre-fracture permeability k_0 is lower than the threshold k_{cr} , pore pressure may increase after a certain degree of compaction. Shaded boxes indicate ranges of k_{cr} for different volcanic systems (refer to Section 4.3 for values and references).

- At Mount Unzen, descriptions of fragment-filled fractures are provided by Goto et al. (2008). Viscosity is determined assuming a pre-eruptive temperature of 850 °C (Nakada et al., 2005), a crystal content of ~0.25 (Holtz et al., 2005), and an equilibrium water content. These features are discussed further in Section 6.1.
- At the Mule Creek vent (New Mexico, USA), abundant ash-filled fractures were described by Stasiuk et al. (1996). Typical fracture widths range from 10–50 mm, and Stasiuk et al. (1996) estimate a pre-eruptive temperature around 800 °C, and note a phenocryst content of approximately 5 vol%. Stasiuk et al. (1996) indicate that the conduit-dwelling rhyolitic magma at Mule Creek was initially water-saturated, thus (as an initial condition) C_{eq} is calculated for the relevant depth range (150–1000 m). Indeed, as a result of effective outgassing during magma ascent, the conduit magma water content is thought to have been much lower than the 2.5–3.0 wt% measured in melt inclusions (Stasiuk et al., 1996).
- At Volcán Chaitén, preserved specimens such as that in Fig. 2A highlight that fracture widths may range from around 1 mm to several tens of mm. A pre-eruptive magma temperature of 825 °C was determined by Castro and Dingwell (2009). These features are discussed further in Section 6.1.
- At Torfajökull (Iceland), McGowan (2016) measured water concentrations between 0.08 and 0.16 wt% in tuffisites and the surrounding host obsidian, although some previous estimates have been somewhat higher (~0.27 wt%: Tuffen et al., 2001; ~0.58 wt%: Berlo et al., 2013). Tuffisites were recorded as being typically 1–20 mm in thickness by McGowan (2016), encompassing the values of 13–15 mm reported by Berlo et al. (2013). Berlo et al. (2013) estimate a pre-eruptive temperature of 800 °C, and we assume the rhyolite is aphyric.
- Finally, ash-filled fractures have been frequently observed at Volcán de Colima, as highlighted in previous studies (Kolzenburg et al., 2012; Kendrick et al., 2016; Farquharson et al., 2016b, see also Fig. 2B). Kolzenburg et al. (2012) studied the strength and permeability of tuffisite-bearing andesite, estimating the typical width of such fractures to range between 3 and 50 mm. In a recent study, Kendrick et al. (2016) calculate the relevant viscosity based on a conduit temperature of 940 °C from Reubi et al. (2013) to be in the range $10^{10.8}$ – $10^{11.9}$ Pa·s.

Evidently, different volcanic systems vary greatly in terms of their rheological properties and the typical range of fracture widths observed (Fig. 3). Notably, the influence of crystal and water content may result in significant variability in η/μ . Consequently, this means that different systems have different propensities for pore pressure augmentation and explosive failure. If k_{cr} is high (e.g. Puyehue–Cordón Caulle), the likelihood that it exceeds the initial permeability k_0 is also high. In this case we may expect frequent pressure increases within tuffisites, giving rise to recrudescence or precluding effective sintering. Indeed, this is consistent with general observations at this system: Schipper et al. (2013) report semi-continuous explosive ash-exhausting events during hybrid explosive-effusive activity at Puyehue–Cordón Caulle between 2011 and 2012. Contrastingly, if the value of k_{cr} is very low (e.g. Volcán de Colima, a relatively more crystalline system), there is a strong possibility that the permeability of the host material will lie above this threshold. In this case, significant pore pressure increases are not generally expected. Rather, frequent tuffisite generation should serve to effectively bleed off pressure and reduce the propensity for dome eruptions over time: the conclusion drawn by Kendrick et al. (2016), who investigated the permeability of experimentally sintered andesite and natural tuffisites from Volcán de Colima.

Taken together, the ranges of k_{cr} plotted on Fig. 4 give an indication as to which systems are relatively more effective at shedding

volatiles via subsurface fracturing. Indeed, we can infer that volcanic environments wherein k_{cr} is generally high may be more prone to generating pore overpressures: a key pre-requisite for explosive fragmentation (Papale, 1999; Spieler et al., 2004; Melnik et al., 2005). In concert with the timescale of molecular diffusion, it provides a useful metric with which to quantify the efficiency of fracture-assisted outgassing, based on the physical mechanism of permeability reduction due to fracture healing.

5. Model limitations

Despite the progress made using this model, it must rely on a number of assumptions, which are important to state explicitly. Note that several of these caveats are specifically addressed above.

First, the model assumes that the material within the fractures is juvenile, i.e. it exhibits the same material properties (such as composition) and is under the same environmental conditions (e.g. temperature) as the surrounding material. While the results still hold as long as the granular fracture-fill exhibits homogeneous chemical properties, care should be taken when the fracture material is demonstrably allochthonous. Similarly, the model assumes that the fracture-fill material is itself homogenous in terms of composition, and that the mean particle size is greater than the effective crystal size. Accordingly, we assume that the initial viscosity of the granular material can be described by the model of Hess and Dingwell (1996)—which was developed for rhyolitic melts—in concert with the particle suspension and solubility models of Mueller et al. (2010) and Liu et al. (2005), respectively. The system is further assumed to be isothermal, which therefore precludes the possibility of evolution of the effective viscosity due to heating or cooling processes (e.g. Costa et al., 2007). We note that compaction timescales will be influenced by the particle size distribution within the fracture; potential differences in this parameter are not explicitly accounted for in our model. However, the initial value of ϕ_i (0.40) reflects the volume fraction of randomly close-packed polydisperse granular material.

Compaction is driven by the overburden stress, which is a function of the bulk density of the host material: this is assumed to be homogenous over the lengthscale ℓ . Further, the constant α is taken to equal 2, after Heap et al. (2014). We note that a lower value (0.78) has been previously obtained by Quane et al. (2009) for sintered volcanic ash, and higher values (2.4–5.3) have been determined for sintered glass powders and glass beads (Ducamp and Raj, 1989; Quane and Russell, 2005, respectively). We adopt the value obtained by Heap et al. (2014) as their starting material (polydisperse ash-to lapilli-sized dacitic aggregate with a rhyolitic groundmass) most closely resembles the fragmental volcanic material envisaged in our model. We highlight that these values are always of the order 10^0 , meaning that the results of Eqs. (1), (17), (18) and (19) are relatively insensitive to variations in α . In this model, the time taken for fractures to fill with particulate material is assumed to be negligibly small. While this is appropriate for fracture infill generated locally (i.e. on the fracture planes), in the case of a fracture being filled with allochthonous material there would exist some finite filling time, which is not accounted for in the calculated healing timescales (nevertheless, we anticipate this filling time to be on the order of seconds or minutes, rather than hours or days). Further, the healing timescales discounts the possibility of buffering by gas (e.g. Rust et al., 2004), fracture propping due to clastic deposition of particles (e.g. Heiken et al., 1988; Tuffen and Dingwell, 2005), or fluid flux-driven alteration, corrosion, dissolution, or precipitation processes (e.g. Africano and Bernard, 2000; Edmonds et al., 2003; Witham et al., 2005; Delmelle et al., 2007; Mueller et al., 2017).

A further assumption is that under a constant driving stress—in this case, the overburden pressure—fractures will heal entirely given sufficient time. The model is one-dimensional, so fracture

length perpendicular to the conduit wall is ignored. This means that horizontal fractures of the same width are treated the same, irrespective of whether they have infinite or infinitesimal length. A related assumption is that lateral fluid transport (i.e. along the fracture) is always greater than fluid transport perpendicular to the fracture orientation (i.e. vertically from the fracture to the host material). Thus the limiting factor defining whether the interstitial pore pressure—which is initially defined as hydrostatic—may increase is fluid transport in the vertical direction (addressed by Eq. (16) and the attendant discussion). Eq. (1) assumes that the pressure driving compaction is homogenous over the width of the fracture. Section 4.1 addresses this explicitly. Finally, we highlight that uncertainties arise from choosing certain constituent models over alternatives (for example, the viscosity model of Hess and Dingwell (1996) over the more complex model of Giordano et al. (2008)). However, within the range of relevant p - T conditions, the absolute value of parameters such as η , C_{eq} , or \mathcal{D} tend to be on the same order of magnitude irrespective of the model employed. The MATLAB® code developed in this study is provided as Supplementary Material, affording the user the possibility of substituting or altering functions depending on different scenarios. Despite the inherent assumptions required in empirical modelling of natural processes, much can be gleaned from integrating experimental and observational data into a numerical approach as described herein. The subsequent section investigates this further.

6. A computational tool for volcanologists

As part of the Supplementary Material, a MATLAB® script is presented which combines the series of equations above into a tractable calculation. The flexible algorithm allows a particular system of interest to be defined in order to predict densification timescales and equivalent permeabilities. Input parameters include a uniform magma temperature, a depth range (“fracture window”) of interest, the density and mean width of fractures within the considered depth range, and the crystal cargo of the magma. In actively outgassing fractures, H_2O content may be below the equilibrium value. As such, the MATLAB® script includes the option for to use either the equilibrium solubility solution or define a particular C_{H_2O} value. Given that the precise distribution of fractures within a volcanic system is rarely known, a function is included which randomly positions fractures within the fracture window until the desired fracture density is achieved without overlap. The following subsection draws on literature data for two different volcanoes in order to explore and compare the timescales of permeability evolution in these systems.

6.1. Case studies: Mount Unzen and Volcán Chaitén

A drilling project between 1999 and 2004 recovered cores from the andesitic–dacitic feeder conduit of Mount Unzen, affording an unprecedented description of the subsurface architecture of a polygenetic stratovolcano. Fractures containing variably-sized fragments (ash- to lapilli-sized Nakada et al., 2005) were observed and quantified radiating laterally from the conduit (Goto et al., 2008). These infilled fractures (so called “volcaniclastic veins”) were found to comprise polydisperse granular material petrographically identical to the host material (both coherent and brecciated andesite and dacite). Goto et al. (2008) suggest two stages of vein development: first, fractures were generated in viscous, crystalline magma or the subsolidus host rock. Thereafter, fractures were infilled rapidly as a result of near-in situ fragmentation and granulation, presumably of material derived from the fracture planes. Alteration of the surrounding material indicates that fluids and particles were employed in the fractures at high temperature. Using the fracture density and the mean fracture width (2.2 m^{-1} and 0.035 m , respectively) presented in

Goto et al. (2008), the timescale for which these fractures could provide effective outgassing pathways for magmatic volatiles can be estimated.

The generation of these fractures has been proposed to be mechanically associated with isolated tremor events, recorded within the lava dome to as deep as 1500 m below the central vent of Mount Unzen and preceding the dome-forming eruptive activity of 1991–1995 (Nakada et al., 1999; Goto et al., 2008). Assuming an intermediate initial crystal content of $\Phi = 0.25$ (Holtz et al., 2005; Noguchi et al., 2008), a temperature of 850°C and bulk density of 2500 kg m^{-3} (Nakada et al., 2005), and an initial host rock permeability of $2.6 \times 10^{-17} \text{ m}^2$ (based on $\phi = 0.002$ from Nakada et al. (2005)), total healing timescales of 35–50 min are calculated (Fig. 5A). Fig. 5A shows that equivalent permeability increases significantly upon fracturing (t_0) followed by a sintering-driven permeability reduction. The reduction in equivalent permeability is nonlinear, a function of the two-slope relation of Eq. (6). After approximately 30 min, all fractures have entirely healed and the magma has regained its pre-fractured state, in line with previous estimates of fracture healing timescales at Mount Unzen and elsewhere (Tuffen et al., 2003).

In order to estimate the diffusion timescale $\lambda_{\mathcal{D}}$ in this scenario, we assume a characteristic particle radius of $50 \mu\text{m}$ (Nakada et al., 2005; Goto et al., 2008). Eqs. (16) and (20) thus yield diffusion timescales between around 400 and 5700 s (~ 7 –95 min), depending on the fracture depth (typically, the deeper a fracture, the greater the water content, and the shorter the diffusion time). Further, we calculate the critical permeability k_{cr} after Eq. (19), determining values ranging from 10^{-17} to 10^{-14} m^2 , again dependent on the fracture depth: relatively deeper fractures yield higher values of k_{cr} than their shallow counterparts. To illustrate the concepts described in Section 4.2, we include the calculated $\lambda_{\mathcal{D}}$ and k_{cr} for the shallowest fracture on Fig. 5A (as shallow fractures take longer to heal than deep fractures, shallow fractures may be considered the rate-limiting factor for total healing). In the Mount Unzen scenario, the diffusion timescale is significantly longer than the time taken for total healing of all fractures, indicating that resorption of exsolved water cannot occur effectively during sintering-driven compaction (in shallow fractures). However, the critical permeability threshold lies below the initial permeability of the material, meaning that fluid can escape from the fracture via Darcian flow (the system is thus in the outgassing regime).

The 2008 eruption of Volcán Chaitén produced abundant evidence for fractures in which volcanic particles densified either wholly, to be preserved as dense obsidian, or partially, to be preserved as tuffisites (Castro et al., 2012; Saubin et al., 2016, see also Fig. 2A). The average pre-eruptive temperature of 825°C was determined by Castro and Dingwell (2009). Saubin et al. (2016) use microtextures and chemistry of the tuffisite shown in Fig. 2A to show that it was actively transporting gas and ash between 360 and 210 m depth (prior to its explosive ejection); for our case study we infer a fracture zone from near the surface down to a depth of 500 m.

Castro et al. (2012) measured H_2O diffusion profiles in tuffisite-bearing blocks from Chaitén, and note that—unless tuffisites intersect highly permeable zones within the conduit—very small fracture spacings are required for diffusive degassing from tuffisites to constitute an effective mechanism of gas loss. With this in mind, we can take a fracture density of 250 m^{-1} with a mean spacing on the order of 10^{-3} m as an upper bound on the fracture number and density at Volcán Chaitén. Here, we assume that a fracture width of 10^{-3} m (Berlo et al., 2013) is typical of the system, though as evident in Fig. 2A, fractures may be significantly wider. In this scenario, the deepest fractures heal in a matter of seconds, while shallow fracture take up to ~ 50 min to heal, with the equivalent permeability of the system dropping accordingly by up to 12 orders of magnitude (Fig. 5B). This is in agreement with the fracture lifespans considered by, among

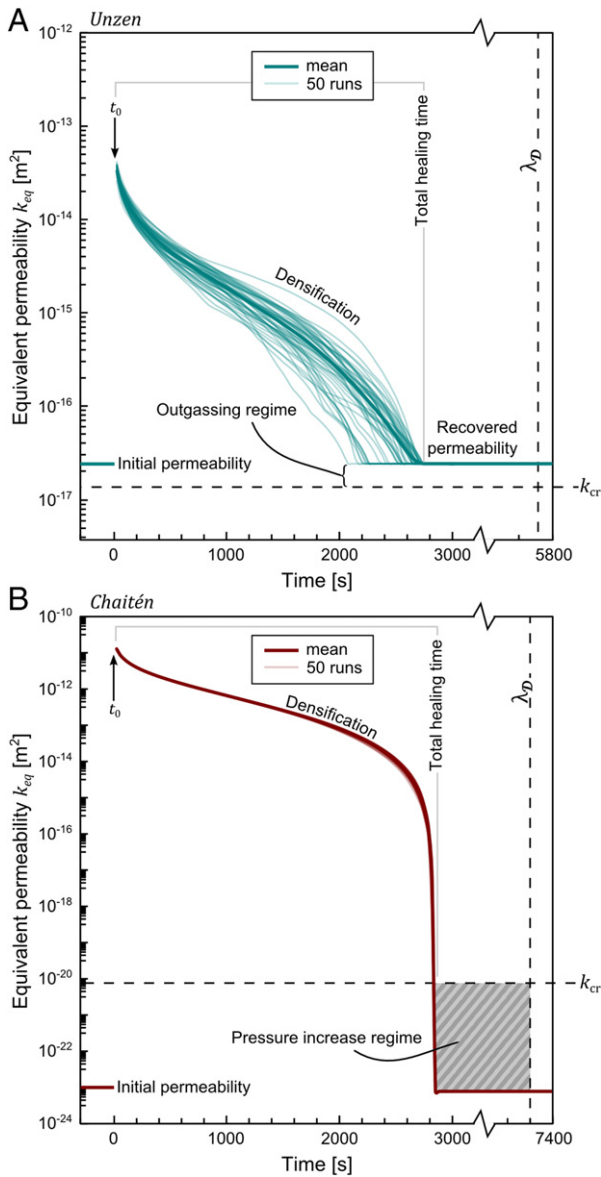


Fig. 5. Permeability evolution for two case studies. A) Permeability evolution calculated using fracture width data for Mount Unzen (see text for references). Total healing time (the time for k_{eq} to return to k_0) is between 35 and 50 min. For the given fracture geometry and effective viscosity (refer to text), critical permeability is around 10^{-17} m^2 , below k_0 . B) Permeability reduction for Chaitén scenario. Total healing time is around 47 min. In this case, k_{cr} ranges between 10^{-18} and 10^{-21} m^2 , meaning that this threshold will be achieved before the complete closure of the fracture system. As the diffusion timescale is greater than the permeability reduction timescale, overpressure can build. Note that either case, only the diffusion timescale λ_D and critical permeability k_{cr} for the shallowest fractures are shown. Permeability evolutions shown are results of 50 randomly generated fracture geometries. Note that the Chaitén case study exhibits less variability in terms of the permeability evolution path. This is a function of the relatively smaller fracture spacing in this example: smaller spacing results in fewer potential fracture distributions, hence less inherent stochasticity.

others, Tuffen et al. (2003), Castro et al. (2012), Berlo et al. (2013), and Saubin et al. (2016), who derive timescales ranging from ~ 10 min to 1 day. As with the Mount Unzen scenario, we calculate the diffusion timescales after Eqs. (16) and (20), and the critical permeability using Eq. (19). Values of λ_D are between around 350 and 2600 s ($\sim 6\text{--}43$ min) using a characteristic particle radius of $30 \mu\text{m}$ (Saubin et al., 2016), while k_{cr} is determined to be on the order 10^{-21} to 10^{-18} m^2 , depending on the fracture depth. We plot the diffusion timescale and critical permeability of the shallowest fracture in

Fig. 5B. Notably, the diffusion timescale is significantly longer than the predicted healing time (as in the Mount Unzen case: Fig. 5A). However, the critical permeability threshold k_{cr} lies above the initial permeability k_0 and the condition $\lambda_{Da} > \lambda_D > \lambda_C$ is fulfilled, placing the system in the pressure increase regime.

Despite exhibiting comparable healing timespans, our model predicts disparate behaviour from the two case study systems—Mount Unzen and Chaitén—arising from different gas evolution mechanisms, with some important distinctions highlighted in Fig. 5. In Fig. 5A (the Mount Unzen case), a low density of relatively wide fractures transiently increases the equivalent permeability of the system by ~ 4 orders of magnitude. In Fig. 5B (the Chaitén case), thin but abundant fractures (representative of a heavily brecciated conduit margin, for example) increases the equivalent permeability of an essentially impermeable host material to almost 10^{-10} m^2 , constituting extremely effective potential routes for gas and ash escape until the shallowest fractures begin to heal, after which the permeability of the system drops off swiftly. Such a rapid permeability shut-off will facilitate pressure increase within densifying magma.

Pressure build-up is compounded by the evolution of fracture permeabilities relative to the critical permeability. For Mount Unzen (Fig. 5A) it is evident that the threshold $k_{f_j} = k_{cr}$ will not be achieved, k_{cr} being lower than the initial permeability. Ultimately, this means that fractures will tend to heal entirely, with volatiles being actively outgassed from magma via Darcian flow. In the Chaitén scenario however (Fig. 5B), the depth-dependent values of k_{cr} are around $7 \times 10^{-21} \text{ m}^2$ and higher. During the final stages of sintering, fracture permeabilities in the Chaitén scenario will intersect this value, even when the mean fracture width is very narrow. Due to the long diffusion timescale relative to the permeability reduction timescale (Fig. 5B), this will inevitably lead to an increase in pore pressure which may promote additional fracturing—evidence of which has been observed within partially-sintered fractures at Chaitén (Saubin et al., 2016) as well as in other volcanic environments (Tuffen et al., 2003)—or may result in more violent explosive failure. Indeed, field and experimental evidence (Saubin et al., 2016) highlights that pressurisation can cause tuffisites—nominally effective at venting magmatic volatiles and promoting quiescent behaviour—to be forcibly ejected from depth during Vulcanian explosions.

6.2. Perspectives

Volcanoes are inherently capricious, not least due to the potential for rapid and significant evolution of permeability in space and time. Accounting for permeability variation in the upper conduit and edifice is a fundamental challenge for the development of gas evolution models that more closely reflect nature (e.g. Collombet, 2009; Collinson and Neuberg, 2012; Saubin et al., 2016). Here we outline a step towards integrating numerical modelling, field observations, and experimental data in a coherent and useful manner. We acknowledge that the relatively simple model presented here may not fully capture the complexities of outgassing from volcanic conduits: for example, the approach outlined herein neglects gas input to the system (or assumes a steady-state condition whereby the fluid inputs and outputs of the fracture system are equal and the gas volume is thus constant). A valuable development of the model would be to incorporate the capacity for volumetric increase or decrease of the gas phase, or to allow for the initial pore fluid condition to be non-hydrostatic. Nevertheless, the combination of porosity and permeability reduction timescales with a parallel layer flow model provides a useful tool with which to estimate the evolution of permeability in volcanic systems over time. With certain caveats, the parallel layer model allows the upscaling of laboratory observations to field-scale, offering information on the expected healing and permeability reduction timescales of zones of fractured magma. Moreover, the determination of a critical permeability threshold and

the typical diffusion timescale of magmatic water affords a diagnostic tool to explain whether or not pore pressures will be prone to increase in a fractured volcanic system, as illustrated in Fig. 4. We highlight that there exists scope for the inclusion of a range of geophysical and geochemical data in the model in order to base the computations on reasonable values. For example, Neuberg et al. (2006) investigated low-frequency volcanic earthquakes in order to argue for a seismogenic fracture zone at 1500 m depth in the conduit of Soufrière Hills Volcano, Montserrat. Modelling fluid flow in the conduit, Thomas and Neuberg (2012) reproduced this seismogenic fracturing at 830 m depth (or at 1500 m depth if they invoked a conduit constriction from dyke to pipe geometry), indicating a critical depth whereat magma fracture is associated with high ascent rates at the conduit wall. As well as scientific drilling, the investigation of otherwise dissected conduits, and the examination of fracture-bearing ejecta—each critical to further our understanding of sub-surface permeable architectures in volcanic environments—this method offers a potential avenue by which to incorporate realistic depth ranges for the “fracture window”. Further, experimental studies of porosity and permeability reduction under volcanically-relevant conditions (e.g. Okumura and Sasaki, 2014; Heap et al., 2015) are fundamental in underpinning the relative evolution of these physical properties during periods of activity and repose. Other promising fields are the combination of permeability evolution models with monitored volumes and timescales of gas emission, which can be used to estimate the bulk system permeability at actively outgassing volcanoes (e.g. Edmonds et al., 2003).

7. Conclusions

The efficiency of fracture-assisted outgassing depends on the width and spatial distribution of infilled fractures (i.e. tuffisites) in a given volcanic system, the timescales over which they are operative, and the permeability of the surrounding material. We define three primary mechanisms governing interstitial pore fluid pressure in a sintering fracture system: compaction, outgassing, and volatile resorption. These operate over different timescales, and the respective ratios of these are thereafter used to define whether the a fracture system is in one of three states:

1. the *outgassing* regime
2. the *diffusive relaxation* regime, and
3. the *pore pressure increase* regime.

Significantly, a critical permeability threshold k_{cr} is also defined, determined using fracture geometry and effective viscosity parameters, which dictates whether a given volcanic fracture system is in the outgassing regime or otherwise. If fracture outgassing is inefficient, the system may be in either of the other two states. We can distinguish which by then comparing the (potential) time taken for complete fracture healing and the time required for resorption of the interstitial exsolved gas phase within the fractures.

Literature data pertaining to two case studies, Mount Unzen and Volcán Chaitén, show that this model can not only predict timescales over which permeability will evolve, but also—crucially—highlights a fundamental difference in their propensities for pore pressure build-up during fracture-healing cycles. In a permeable system, fractures may provide effective outgassing pathways, which will heal over time until the system retains its original permeability. In a low-permeability system, fractures will similarly yield a highly efficient outgassing mechanism. However, pore pressure will increase as the decreasing fracture permeability intersects the critical permeability (a function of the effective viscosity and the mean fracture width). This means that either (1) the system will not achieve its pre-fracture permeability or (2) the system will be driven inexorably towards explosive failure. Literature data is used to determine the ranges of

the critical permeability threshold for six silicic volcanoes: Puyehue–Cordón Caulle, Mount Unzen, Mule Creek, Chaitén, Torfajökull, and Volcán de Colima. Notably, the wide span of their critical values reflects the spectrum of eruptive activity observed at these systems.

Acknowledgments

We thank Luke Griffiths, Alexandra Kushnir, and Jérémie Vasseur. JIF and MJH acknowledge an Initiative d'Excellence (IDEX) “Contrats Doctoraux” grant and an IDEX “Attractivité” grant (VOLPERM), respectively (both funded by the University of Strasbourg). MJH also acknowledges funding from CNRS-INSU grant “Permeability reduction in densifying magma”. This work has been published under the framework of LABEX grant ANR-11-LABX-0050_G-EAU-THERMIE-PROFONDE and so benefits from state funding managed by the Agence Nationale de la Recherche (ANR) as part of the “Investissements d'avenir” program. FBW acknowledges funding from Advanced grant (Explosive Volcanism in the Earth System: Experimental Insights; EVOKES, 247076). Amy Ryan and an anonymous reviewer are thanked for their constructive feedback. Hugh Tuffen and an anonymous reviewer are thanked for comments on a previous draft of this manuscript.

The MATLAB® program described herein can be downloaded at: <https://figshare.com/s/c5ff28905ed1ba93a19b>.

Appendix A

A.1. The basic equation for water viscosity

The viscosity μ of water vapour (the interstitial pore fluid) is an important parameter considered in the main text; it is however non-trivial to constrain. This following appendix outlines the governing principles and equations employed in order to calculate within the `FRACKR.m` model. The equations and coefficients are derived from the Industrial Formulation IAPWS-IF97 for the thermodynamic properties of water and steam as described in Wagner et al. (2000), and in subsequent updates from The International Association for the Properties of Water and Steam: IAPWS (2008, 2012, 2014).

Fluid viscosity μ is a function of temperature T and fluid density ρ . The former is established in our model as a user-defined run condition, and the latter is calculated as functions of pressure p , temperature T , enthalpy h , and R (an Ideal Gas constant). The p - T condition-dependent relations of these parameters are described in subsequent sections of this appendix. Note that p corresponds the depth of each individual fracture (equivalent to the stress driving compaction), given in MPa such that $p = \sigma_{zz}/10^6$, where σ_{zz} is the vertical compaction pressure in Pa as defined as in the main text. Temperature is given hereafter in K ($^{\circ}\text{C} + 273.15$).

Normalised fluid viscosity is given here by Ω , a function of the fluid viscosity μ and a reference value μ^* equal to 1.00×10^{-6} Pa·s:

$$\Omega = \frac{\mu}{\mu^*} = \underbrace{\left[\frac{100\sqrt{\theta}}{\sum_{i=0}^3 \frac{H_i}{\theta^i}} \right]}_{\mu_0} \times \underbrace{\left[\varrho \sum_{i=0}^5 \left(\frac{1}{\theta} - 1 \right)^i \sum_{j=0}^6 H_{i,j} (\varrho - 1)^j \right]}_{\mu_1} \times \underbrace{\left[1 \right]}_{\mu_2} \quad (\text{A.1})$$

where $\theta = T/T^*$ and $\varrho = \rho/\rho^*$ are dimensionless values of temperature and density, with T^* and ρ^* being reference values of either property (647.096 K and 322.0 kg m^{-3} , respectively). The factor μ_0 corresponds to the viscosity in the dilute-gas limit, while the second factor μ_1 accounts for the contribution to viscosity of finite density. The final component μ_2 is the critical enhancement of viscosity, which is valid only in a very small region around the critical point

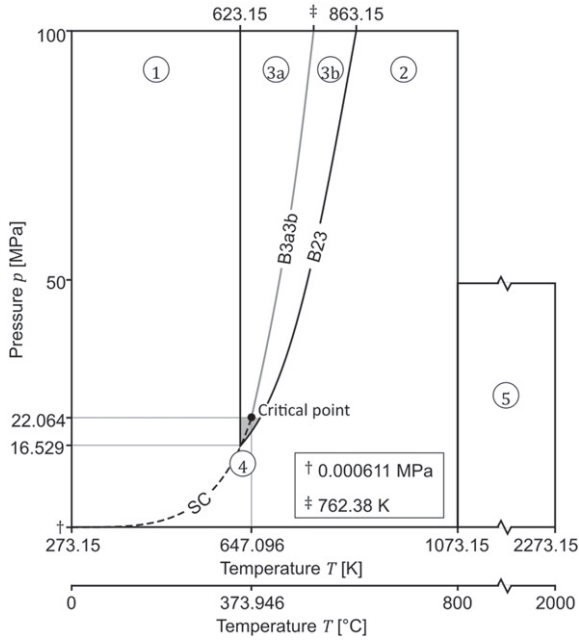


Fig. A.6. Simplified vapour-phase diagram for water, shown in p - T space. B_{23} indicates the boundary between regions 2 and 3. Region 3 is sub-divided into sub-regions 3a and 3b, which are delineated by the boundary B_{3a3b} . The dashed line SC represents the saturation curve. Note values † and ‡, given in the legend. Source: Modified after Wagner et al. (2000)

of water (647.096 K; 22.064 MPa; Fig. A.6). Because the influence of μ_2 is negligible other than near to the critical point, it is neglected herein (i.e. μ_2 is normalised to 1). Values for coefficients H_i and H_{ij} are given in Tables A.2 and A.3, respectively.

Throughout this appendix, the properties temperature T , pressure p , density ρ , enthalpy h , and specific volume v are often expressed as dimensionless parameters. These take the form $\theta = T/T^*$; $\tau = T^*/T$; $\pi = p/p^*$; $\varrho = \rho/\rho^*$; $h = h/h^*$, and $\omega = v/v^*$. In each case, the superscript * indicates a reference value. Reference values pertinent to the succeeding equations are defined throughout the text.

A.2. Thermodynamic regions

The thermodynamic properties of water—such as ρ , μ , h —vary as functions of p and T . In discrete p - T domains, termed “regions”, these properties are described by region-specific basic equations. Fig. A.6 illustrates how these regions are distinguished.

Region 1 is defined as p - T conditions whereby $273.15 < T < 623.15$ and p is greater than the saturation pressure, defined as a function of temperature such that:

$$p = \left[\frac{20}{-N + \sqrt{N^2 - 4MO}} \right]^4 ; \begin{cases} M = \vartheta^2 + n_1 \vartheta + n_2 \\ N = n_3 \vartheta^2 + n_4 \vartheta + n_5 \\ O = n_6 \vartheta^2 + n_7 \vartheta + n_8 \end{cases} \quad (\text{A.2})$$

Table A.2
List of coefficients for Eq. (A.1) (μ_0) from IAPWS (2008).

i	H_i
0	0.167752×10^1
1	0.220462×10^1
2	0.6366564
3	-0.241605

Table A.3
List of coefficients for Eq. (A.1) (μ_1) from IAPWS (2008).

i	J	H_{ij}	i	J	H_{ij}
0	0	5.20094×10^1	0	2	-2.81378×10^1
1	0	8.50895×10^2	1	2	-9.06851×10^1
2	0	-1.08374	2	2	-7.72479×10^1
3	0	-2.89555×10^1	3	2	-4.89837×10^1
0	1	2.22531×10^1	4	2	-2.57040×10^1
1	1	9.99115×10^1	0	3	1.61913×10^1
2	1	1.88797	1	3	2.57399×10^1
3	1	1.26613	0	4	-3.25372×10^2
5	1	1.20573×10^1	3	4	6.98452×10^2

Table A.4
List of coefficients for Eq. (A.2) (μ_1) from IAPWS (2012).

i	n_i
1	$0.11670521452767 \times 10^4$
2	$-0.72421316703206 \times 10^6$
3	$-0.17073846940092 \times 10^2$
4	$0.12020824702470 \times 10^5$
5	$-0.32325550322333 \times 10^7$
6	$0.14915108613530 \times 10^2$
7	$-0.48232657361591 \times 10^4$
8	$0.40511340542057 \times 10^6$
9	-0.23855557567849
10	$0.65017534844798 \times 10^3$

where $\vartheta = T + n_9/(T - n_{10})$ and coefficients $n_1 \dots n_{10}$ are given in Table A.4. Note that Eq. (A.2) is the equation of the saturation curve (SC; Fig. A.6).

Region 3 is defined as the p - T domain wherein $T \geq 623.15$ K and $p > B_{23}$ (as a function of temperature). B_{23} is the boundary between regions 2 and 3, and is defined thus:

$$\pi = n_1 + n_2 \theta + n_3 \theta^2 \quad (\text{A.3})$$

where π is dimensionless pressure described by p/p^* , where $p^* = 1$ MPa. As previously, $\theta = T/T^*$, however the reference value in this case is $T^* = 1$ K. Coefficients $n_1 \dots n_3$ are given in Table A.5. Region 3 is also subdivided into sub-regions 3a and 3b, which is described in a following section.

Region 4 is defined as the immediate conditions around the saturation curve (Eq. (A.2); SC on Fig. A.6). For the purposes of this model, p - T conditions are classified as region 4 when the absolute difference between p and the saturation pressure is less than 10^{-5} .

Region 5 is defined as any p - T conditions whereby $0.000611 < p \leq 50$ MPa and $1073.15 < T \leq 2273.15$ K.

Region 2 is defined wherever $16.529 < p \leq 100$ MPa and $T > B_{23}$ (as a function of pressure) and where $0.000611 < p \leq 16.529$ MPa and $T > SC$ (the saturation curve; Fig. A.6). In practice, region 2 is allocated last, to any valid p - T conditions once all other potential regions (1, 3–5) have been exhausted.

Table A.5
List of coefficients for Eq. (A.3) (μ_1) from IAPWS (2012).

i	n_i
1	$0.34805185628969 \times 10^3$
2	$-0.11671859879975 \times 10^1$
3	$0.10192970039326 \times 10^{-2}$
4	$0.57254459862746 \times 10^3$
5	$0.13918839778870 \times 10^2$

Table A.6
List of coefficients for Eqs. (A.4) and (A.9) from IAPWS (2012).

i	I_i	J_i	n_i	i	I_i	J_i	n_i
1	0	-2	0.14632971213167	18	2	3	-0.44141845330846 × 10 ⁻⁵
2	0	-1	-0.84548187169114	19	2	17	-0.72694996297594 × 10 ⁻¹⁵
3	0	0	-0.37563603672040 × 10 ¹	20	3	-4	-0.31679644845054 × 10 ⁻⁴
4	0	1	0.33855169168385 × 10 ¹	21	3	0	-0.28270797985312 × 10 ⁻⁵
5	0	2	-0.95791963387872	22	3	6	-0.85205128120103 × 10 ⁻⁹
6	0	3	0.15772038513228	23	4	-5	-0.22425281908000 × 10 ⁻⁵
7	0	4	-0.16616417199501 × 10 ⁻¹	24	4	-2	-0.65171222895601 × 10 ⁻⁶
8	0	5	0.81214629983568 × 10 ⁻³	25	4	10	-0.14341729937924 × 10 ⁻¹²
9	1	-9	0.28319080123804 × 10 ⁻³	26	5	-8	-0.40516996860117 × 10 ⁻⁶
10	1	-7	-0.60706301565874 × 10 ⁻³	27	8	-11	-0.12734301741641 × 10 ⁻⁸
11	1	-1	-0.18990068218419 × 10 ⁻¹	28	8	-6	-0.17424871230634 × 10 ⁻⁹
12	1	0	-0.32529748770505 × 10 ⁻¹	29	21	-29	-0.68762131295531 × 10 ⁻¹⁸
13	1	1	-0.21841717175414 × 10 ⁻¹	30	23	-31	0.14478307828521 × 10 ⁻¹⁹
14	1	3	-0.52838357969930 × 10 ⁻⁴	31	29	-38	0.26335781662795 × 10 ⁻²²
15	2	-3	-0.47184321073267 × 10 ⁻³	32	30	-39	-0.11947622640071 × 10 ⁻²²
16	2	0	-0.30001780793026 × 10 ⁻³	33	31	-40	0.18228094581404 × 10 ⁻²³
17	2	1	0.47661393906987 × 10 ⁻⁴	34	32	-41	-0.93537087292458 × 10 ⁻²⁵

A.3. Pore fluid density

In order to determine the viscosity of water under the imposed pressure and temperature conditions for each fracture of the model, the fluid density must first be calculated. Fluid density is the reciprocal of the specific volume of a gas v , which is calculated slightly differently in each of the regions 1, 2, 3, and 5. Due to the negligible extent of p - T space encompassed by region 4, the governing basic equations for this region are ignored. Any fracture value coinciding with the saturation curve will return a NaN (not a number) value.

In regions 1, 2, and 5, the basic equation are formulations for the specific Gibbs free energy G , given here in dimensionless form such that $g = G/RT$, where R is the specific gas constant of water (0.461526 kJ kg⁻¹ K⁻¹) and T is temperature in K.

A.3.1. Region 1

The pressure- and temperature-dependent relationship of specific volume in region 1 is here denoted v_1 , and is determined after IAPWS (2012) such that:

$$v_1(\pi, \tau) = \frac{RT}{p} \pi \left[\sum_{i=1}^{34} -n_i I_i (7.1 - \pi)^{I_i - 1} (\tau - 1.222)^{J_i} \right] \quad (A.4)$$

Table A.7
List of coefficients for Eqs. (A.5) and (A.10) from IAPWS (2012).

J	I_j	J_j	n_j	J	I_j	J_j	n_j
1	1	0	-0.17731742473213 × 10 ⁻²	23	7	0	-0.59059564324270 × 10 ⁻¹⁷
2	1	1	-0.17834862292358 × 10 ⁻¹	24	7	11	-0.12621808899101 × 10 ⁻⁵
3	1	2	-0.45996013696365 × 10 ⁻¹	25	7	25	-0.38946842435739 × 10 ⁻¹
4	1	3	-0.57581259083432 × 10 ⁻¹	26	8	8	0.11256211360459 × 10 ⁻¹⁰
5	1	6	-0.50325278727930 × 10 ⁻¹	27	8	36	-0.82311340897998 × 10 ¹
6	2	1	-0.33032641670203 × 10 ⁻⁴	28	9	13	0.19809712802088 × 10 ⁻⁷
7	2	2	-0.18948987516315 × 10 ⁻³	29	10	4	0.10406965210174 × 10 ⁻¹⁸
8	2	4	-0.39392777243355 × 10 ⁻²	30	10	10	-0.10234747095929 × 10 ⁻¹²
9	2	7	-0.43797295650573 × 10 ⁻¹	31	10	14	-0.10018179379511 × 10 ⁻⁸
10	2	36	-0.26674547914087 × 10 ⁻⁴	32	16	29	-0.80882908646985 × 10 ⁻¹⁰
11	3	0	0.20481737692309 × 10 ⁻⁷	33	16	50	0.10693031879409
12	3	1	0.43870667284435 × 10 ⁻⁶	34	18	57	-0.33662250574171
13	3	3	-0.32277677238570 × 10 ⁻⁴	35	20	20	0.89185845355421 × 10 ⁻²⁴
14	3	6	-0.15033924542148 × 10 ⁻²	36	20	35	0.30629316876232 × 10 ⁻¹²
15	3	35	-0.40668253562649 × 10 ⁻¹	37	20	48	-0.42002467698208 × 10 ⁻⁵
16	4	1	-0.78847309559367 × 10 ⁻⁹	38	21	21	-0.59056029685639 × 10 ⁻²⁵
17	4	2	0.12790717852285 × 10 ⁻⁷	39	22	53	0.37826947613457 × 10 ⁻⁵
18	4	3	0.48225372718507 × 10 ⁻⁶	40	23	39	-0.12768608934681 × 10 ⁻¹⁴
19	5	7	0.22922076337661 × 10 ⁻⁵	41	24	26	0.73087610595061 × 10 ⁻²⁸
20	6	3	-0.16714766451061 × 10 ⁻¹⁰	42	24	40	0.55414715350778 × 10 ⁻¹⁶
21	6	16	-0.21171472321355 × 10 ⁻²	43	24	58	-0.94369707241210 × 10 ⁻⁶
22	6	35	-0.23895741934104 × 10 ²				

where T^* and p^* are 1386 K and 16.53 MPa, respectively. Values for coefficient i are given in Table A.6.

Fluid density is then given by $\rho = v_1^{-1}$.

A.3.2. Region 2

The pressure- and temperature-dependent relationship of specific volume in region 2 is here denoted v_2 , comprising an Ideal Gas part g_π and a residual part g_π^r (IAPWS, 2012):

$$v_2(\pi, \tau) = \frac{RT}{p} \pi \left(\underbrace{\left[\frac{1}{\pi} \right]}_{g_\pi^r} + \underbrace{\left[\sum_{j=1}^{43} n_j I_j \pi^{I_j - 1} (\tau - 0.5)^{J_j} \right]}_{g_\pi^r} \right) \quad (A.5)$$

where T^* and p^* are 540 K and 1 MPa, respectively. Coefficient values are given in Table A.7.

Fluid density is then given by $\rho = v_2^{-1}$.

A.3.3. Region 3

In region 3, the basic equation is that of the specific Helmholtz free energy f , given here in its dimensionless form $\tilde{f} = f/RT$, where R

Table A.8
List of coefficients for Eq. (A.8) from IAPWS (2014).

<i>i</i>	<i>n_i</i>
1	0.201464004206875 × 10 ⁴
2	0.374696550136983 × 10 ¹
3	−0.219921901054187 × 10 ^{−1}
4	0.87513168600995 × 10 ^{−4}

and *T* are as previously defined:

$$f(\varrho, \tau) = n_1 \ln \varrho + \sum_{i=2}^{40} n_i \varrho^i \tau^i \quad (A.6)$$

Specific volume cannot be determined explicitly from Eq. (A.6). However, it can be determined as a function of specific enthalpy *h*, which is given here in its dimensionless form *h*₁:

$$h = \frac{h}{RT} = \tau \left[\sum_{i=2}^{40} n_i \varrho^i J_i \tau^{i-1} \right] + \varrho \left[n_1/\varrho + \sum_{j=2}^{40} n_j J_j \varrho^{j-1} \tau^j \right] \quad (A.7)$$

Region 3 is subdivided into sub-regions 3a and 3b by the isentropic curve *B*_{3a3b} (Fig. A.6), which is related to the dimensionless form of enthalpy *h* in the following manner:

$$h_{ab} = \frac{h}{h^*} = n_1 + n_2 \pi + n_3 \pi^2 + n_4 \pi^3 \quad (A.8)$$

where $\pi = p/p^*$, with $h^* = 1 \text{ kJ kg}^{-1}$ and $p^* = 1 \text{ MPa}$. Coefficients $n_1 \dots n_4$ are given in Table A.8.

As enthalpy in region 3 is not described explicitly as a function of pressure and temperature according to IAPWS, this value is approximated in our model as the mean values of enthalpy at the boundaries between regions 1 and 3 (Eq. (A.9)), and between regions 3 and 2 (Eq. (A.10)). The values *h*₁ and *h*₂ are calculated thus:

$$h_1 = RT \cdot \tau \left[\sum_{i=1}^{34} n_i (7.1 - \pi)^i J_i (\tau - 1.222)^{i-1} \right] \quad (A.9)$$

where $p^* = 16.53 \text{ MPa}$, $T^* = 1386 \text{ K}$, and the limit temperature *T* is 623.15 K, and

$$h_2 = RT \cdot \tau \left(\underbrace{\left[\sum_{i=1}^9 n_i^0 J_i^0 \tau^{i-1} \right]}_{g_r^0} + \underbrace{\left[\sum_{j=1}^{43} n_j \pi^j J_j (\tau - 0.5)^{j-1} \right]}_{g_r^1} \right) \quad (A.10)$$

where $p^* = 1 \text{ MPa}$, $T^* = 540 \text{ K}$, and the limit temperature *T* is a function of pressure:

$$T = \frac{\theta}{T^*} = n_4 + \left(\frac{\pi - n_5}{n_3} \right)^{\frac{1}{2}} \quad (A.11)$$

with $T^* = 1 \text{ K}$ and $p^* = 1 \text{ MPa}$. The coefficients $n_3 \dots n_5$ are as defined in Table A.4. Note that Eq. (A.11) is simply the *B*₂₃ boundary equation (Eq. (A.3)) expressed in terms of temperature. Coefficients for Eq. (A.9) are given in Table A.6. Eq. (A.10) is separated into an Ideal Gas part *g*_r⁰ and residual part *g*_r¹. Coefficients for the former are given in Eq. (A.11). Coefficients for the latter are given in Table A.7.

Thus we approximate enthalpy by $h = (h_1 + h_2)/2$. Note that this approximation is applied to all *p*–*T* conditions comprising region 3. In actuality, however, those parts of sub-regions 3a and 3b where $16.529 \leq p \leq 22.064$ (the shaded region of Fig. A.6) lie below the critical point and would incur additional complexity in terms of estimating enthalpy (water may exist in its liquid or gaseous phase). Nevertheless, this intricacy is ignored for the sake of simplicity. If $h < h_{ab}$, the imposed *p*–*T* conditions are defined as sub-region 3a, and if $h \geq h_{ab}$ then the system is defined as sub-region 3b. The normalised specific volume for each sub-region— ω_{3a} and ω_{3b} , respectively—is thereafter described by (IAPWS, 2014):

$$\omega_{3a} = \frac{v}{v^*} = \sum_{i=1}^{32} n_i (\pi + 0.1280)^i (h - 0.727)^i \quad (A.12)$$

Table A.9
List of coefficients for Eq. (A.10) from IAPWS (2012).

<i>i</i>	<i>J_i⁰</i>	<i>n_i⁰</i>	<i>i</i>	<i>J_i⁰</i>	<i>n_i⁰</i>
1	0	−0.96927686500217 × 10 ¹	6	−2	0.14240819171444 × 10 ¹
2	1	0.10086655968018 × 10 ²	7	−1	−0.43839511319450 × 10 ¹
3	−5	−0.56087911283020 × 10 ^{−2}	8	2	−0.28408632460772
4	−4	0.71452738081455 × 10 ^{−1}	9	3	0.21268463753307 × 10 ^{−1}
5	−3	−0.40710498223928			

Table A.10
List of coefficients for Eq. (A.12) from IAPWS (2014).

<i>i</i>	<i>I_i</i>	<i>J_i</i>	<i>n_i</i>	<i>i</i>	<i>I_i</i>	<i>J_i</i>	<i>n_i</i>
1	−12	6	0.529944062966028 × 10 ^{−2}	17	−2	16	0.568366875815960 × 10 ⁴
2	−12	8	−0.170099690234461	19	−1	0	0.808169540124668 × 10 ^{−2}
3	−12	12	0.111323814312927 × 10 ²	19	−1	1	0.172416341519307
4	−12	18	−0.217898123145125 × 10 ⁴	20	−1	2	0.104270175292927 × 10 ¹
5	−10	4	−0.506061827980875 × 10 ^{−3}	21	−1	3	−0.297691372792847
6	−10	7	0.556495239685324	22	0	0	0.560394465163593
7	−10	10	−0.943672726094016 × 10 ¹	23	0	1	0.275234661176914
8	−8	5	−0.297856807561527	24	1	0	−0.148347894866012
9	−8	12	0.939353943717186 × 10 ²	25	1	1	−0.651142513478515 × 10 ^{−1}
10	−6	3	0.192944939465981 × 10 ^{−1}	26	1	2	−0.292468715386302 × 10 ¹
11	−6	4	0.421740664704763	27	2	0	0.664876096952665 × 10 ^{−1}
12	−6	22	−0.368914126282330 × 10 ⁷	28	2	2	0.352335014263844 × 10 ¹
13	−4	2	−0.737566847600639 × 10 ^{−2}	29	3	0	−0.146340792313332 × 10 ^{−1}
14	−4	3	−0.354753242424366	30	4	2	−0.224503486668184 × 10 ¹
15	−3	7	−0.199768169338727 × 10 ¹	31	5	2	0.110533464706142 × 10 ¹
16	−2	3	0.115456297059049 × 10 ¹	32	8	2	−0.408757344495612 × 10 ^{−1}

Table A.11

List of coefficients for Eq. (A.13) from IAPWS (2014).

J	I_J	J_J	n_J	J	I_J	J_J	n_J
1	-12	0	$-0.225196934336318 \times 10^{-8}$	16	-4	6	$-0.321087965668917 \times 10^1$
2	-12	1	$0.140674363313486 \times 10^{-7}$	17	-4	10	$0.607567815637771 \times 10^3$
3	-8	0	$0.233784085280560 \times 10^{-5}$	18	-3	0	$0.557686450685932 \times 10^{-3}$
4	-8	1	$-0.331833715229001 \times 10^{-4}$	19	-3	2	0.187499040029550
5	-8	3	$0.107956778514318 \times 10^{-2}$	20	-2	1	$0.905368030448107 \times 10^{-2}$
6	-8	6	-0.271382067378863	21	-2	2	0.285417173048685
7	-8	7	$0.107202262490333 \times 10^1$	22	-1	0	$0.329924030996098 \times 10^{-1}$
8	-8	8	-0.853821329075382	23	-1	1	0.239897419685483
9	-6	0	$-0.215214194340526 \times 10^{-4}$	24	-1	4	$0.482754995951394 \times 10^1$
10	-6	1	$0.769656088222730 \times 10^{-3}$	25	-1	5	$-0.118035753702231 \times 10^2$
11	-6	2	$-0.431136580433864 \times 10^{-2}$	26	0	0	0.169490044091791
12	-6	5	0.453342167309331	27	1	0	$-0.179967222507787 \times 10^{-1}$
13	-6	6	-0.507749535873652	28	1	1	$0.371810116332674 \times 10^{-1}$
14	-6	10	$-0.100475154528389 \times 10^3$	29	2	2	$-0.536288335065096 \times 10^{-1}$
15	-4	3	-0.219201924648793	30	2	6	$0.160697101092520 \times 10^1$

Table A.12

List of coefficients for Eq. (A.14) from IAPWS (2014).

i	I_i	J_i	n_i
1	1	1	$0.15736404855259 \times 10^{-2}$
2	1	2	$0.90153761673944 \times 10^{-3}$
3	1	3	$-0.50270077677648 \times 10^{-2}$
4	2	3	$0.22440037409485 \times 10^{-5}$
5	2	9	$-0.41163275453471 \times 10^{-5}$
6	3	7	$0.37919454822955 \times 10^{-7}$

where $v^* = 0.0028 \text{ m}^3 \text{ kg}^{-1}$, $p^* = 100$, and $h^* = 2100 \text{ kJ kg}^{-1}$, and

$$\omega_{3b} = \frac{v}{v^*} = \sum_{j=1}^{30} n_j (\pi + 0.00661)^{I_j} (h - 0.720)^{J_j} \quad (\text{A.13})$$

where $v^* = 0.0088 \text{ m}^3 \text{ kg}^{-1}$, $p^* = 100$, and $h^* = 2800 \text{ kJ kg}^{-1}$. Coefficient values are given in Tables A.10 and A.11. Fluid density is then given by $\rho = (\omega_{3a} \cdot v^*)^{-1}$ or $\rho = (\omega_{3b} \cdot v^*)^{-1}$, as appropriate.

A.3.4. Region 5

The pressure- and temperature-dependent relationship of specific volume in region 5 is here denoted v_5 , comprising an Ideal Gas part g_r^0 and a residual part g_r^1 (IAPWS, 2012):

$$v_5(\pi, \tau) = \frac{RT}{p} \pi \left(\underbrace{\left[\frac{1}{\pi} \right]}_{g_r^0} + \underbrace{\left[\sum_{j=1}^5 n_j I_j \pi^{I_j - 1} \tau^{J_j} \right]}_{g_r^1} \right) \quad (\text{A.14})$$

where T^* and p^* are 1000 K and 1 MPa, respectively. Coefficient values are given in Table A.12.

Fluid density may then be calculated by $\rho = v_5^{-1}$.

References

- Africano, F., Bernard, A., 2000. Acid alteration in the fumarolic environment of Usu Volcano, Hokkaido, Japan. *J. Volcanol. Geotherm. Res.* 97, 475–495.
- Berlo, K., Tuffen, H., Smith, V., Castro, J., Pyle, D., Mather, T., Geraki, K., 2013. Element variations in rhyolitic magma resulting from gas transport. *Geochim. Cosmochim. Acta* 121, 436–451.
- Castro, J.M., Bindeman, I.N., Tuffen, H., Schipper, C.I., 2014. Explosive origin of silicic lava: textural and $\delta D\text{-H}_2\text{O}$ evidence for pyroclastic degassing during rhyolite effusion. *Earth Planet. Sci. Lett.* 405, 52–61.
- Castro, J.M., Cordonnier, B., Schipper, C.I., Tuffen, H., Baumann, T.S., Feisel, Y., 2016. Rapid laccolith intrusion driven by explosive volcanic eruption. *Nat. Commun.* 7.
- Castro, J.M., Cordonnier, B., Tuffen, H., Tobin, M.J., Puskas, L., Martin, M.C., Bechtel, H.A., 2012. The role of melt-fracture degassing in defusing explosive rhyolite eruptions at Volcán Chaitén. *Earth Planet. Sci. Lett.* 333, 63–69.
- Castro, J.M., Dingwell, D.B., 2009. Rapid ascent of rhyolitic magma at Chaitén Volcano, Chile. *Nature* 461, 780–783.
- Castro, J.M., Schipper, C.I., Mueller, S.P., Militzer, A., Amigo, A., Parejas, C.S., Jacob, D., 2013. Storage and eruption of near-liquidus rhyolite magma at Cordón Caulle, Chile. *Bull. Volcanol.* 75, 702.
- Chevalier, L., Collombet, M., Pinel, V., 2017. Temporal evolution of magma flow and degassing conditions during dome growth, insights from 2d numerical modelling. *J. Volcanol. Geotherm. Res.* 333, 116–133.
- Collinson, A., Neuberg, J., 2012. Gas storage, transport and pressure changes in an evolving permeable volcanic edifice. *J. Volcanol. Geotherm. Res.* 243, 1–13.
- Collombet, M., 2009. Two-dimensional gas loss for silicic magma flows: toward more realistic numerical models. *Geophys. J. Int.* 177, 309–318.
- Costa, A., Melnik, O., Vedeneeva, E., 2007. Thermal effects during magma ascent in conduits. *J. Geophys. Res. Solid Earth* 112.
- Delmelle, P., Lambert, M., Dufrière, Y., Gerin, P., Óskarsson, N., 2007. Gas/aerosol-ash interaction in volcanic plumes: new insights from surface analyses of fine ash particles. *Earth Planet. Sci. Lett.* 259, 159–170.
- Doremus, R., 2000. Diffusion of water in rhyolite glass: diffusion-reaction model. *J. Non-Cryst. Solids* 261, 101–107.
- Ducamp, V., Raj, R., 1989. Shear and densification of glass powder compacts. *J. Am. Ceram. Soc.* 72, 798–804.
- Edmonds, M., Oppenheimer, C., Pyle, D., Herd, R., Thompson, G., 2003. SO_2 emissions from Soufrière Hills volcano and their relationship to conduit permeability, hydrothermal interaction and degassing regime. *J. Volcanol. Geotherm. Res.* 124, 23–43.
- Farquharson, J.I., Heap, M.J., Baud, P., 2016a. Strain-induced permeability increase in volcanic rock. *Geophys. Res. Lett.* 43.
- Farquharson, J.I., Heap, M.J., Lavallée, Y., Varley, N.R., Baud, P., 2016b. Evidence for the development of permeability anisotropy in lava domes and volcanic conduits. *J. Volcanol. Geotherm. Res.* 323, 163–185.
- Farquharson, J.I., Heap, M.J., Varley, N.R., Baud, P., Reuschlé, T., 2015a. Permeability and porosity relationships of edifice-forming andesites: a combined field and laboratory study. *J. Volcanol. Geotherm. Res.* 297, 52–68.
- Farquharson, J.I., James, M., Tuffen, H., 2015b. Examining rhyolite lava flow dynamics through photo-based 3d reconstructions of the 2011–2012 lava flowfield at Cordón-Caulle, Chile. *J. Volcanol. Geotherm. Res.* 304, 336–348.
- Giordano, D., Russell, J.K., Dingwell, D.B., 2008. Viscosity of magmatic liquids: a model. *Earth and Planetary Science Letters* 271, 123–134.
- Gonnermann, H., Manga, M., 2003. Explosive volcanism may not be an inevitable consequence of magma fragmentation. *Nature* 426, 432–435.
- Goto, Y., Nakada, S., Kurokawa, M., Shimano, T., Sugimoto, T., Sakuma, S., Hoshizumi, H., Yoshimoto, M., Uto, K., 2008. Character and origin of lithofacies in the conduit of Unzen Volcano, Japan. *J. Volcanol. Geotherm. Res.* 175, 45–59.
- Heap, M., Farquharson, J.I., Wadsworth, F., Kolzenburg, S., Russell, J., 2015. Timescales for permeability reduction and strength recovery in densifying magma. *Earth Planet. Sci. Lett.* 429, 223–233.
- Heap, M., Kolzenburg, S., Russell, J., Campbell, M., Welles, J., Farquharson, J., Ryan, A., 2014. Conditions and timescales for welding block-and-ash flow deposits. *J. Volcanol. Geotherm. Res.* 289, 202–209.
- Heap, M.J., Kennedy, B.M., 2016. Exploring the scale-dependent permeability of fractured andesite. *Earth Planet. Sci. Lett.* 447, 139–150.
- Heiken, G., Wohletz, K., Eichelberger, J., 1988. Fracture fillings and intrusive pyroclasts, Inyo Domes, California. *J. Geophys. Res. Solid Earth* 93, 4335–4350.
- Hess, K., Dingwell, D., 1996. Viscosities of hydrous leucogranitic melts: a non-Arrhenian model. *Am. Mineral.* 81, 1297–1300.
- Holloway, J., 1981. Volatile interactions in magmas. *Thermodynamics of minerals and melts*. Springer, pp. 273–293.
- Holtz, F., Sato, H., Lewis, J., Behrens, H., Nakada, S., 2005. Experimental petrology of the 1991–1995 Unzen Dacite, Japan. Part i: phase relations, phase composition and pre-eruptive conditions. *J. Petrol.* 46, 319–337.
- IAPWS, 2008. Release on the IAPWS formulation 2008 for the viscosity of ordinary water substance. IAWPS meeting September 2008. Technical Report. Berlin, Germany.

- IAPWS, 2012. Revised release on the iapws industrial formulation 1997 for the thermodynamic properties of water and steam. IAPWS meeting August 2007. Technical Report. Lucerne, Switzerland.
- IAPWS, 2014. Revised supplementary release on backward equations for the functions $t(p, h)$, $v(p, h)$ and $t(p, s)$, $v(p, s)$ for region 3 of the iapws industrial formulation 1997 for the thermodynamic properties of water and steam. IAPWS meeting June 2014. Technical Report. Moscow, Russia.
- Jaupart, C., 1998. Gas loss from magmas through conduit walls during eruption. *Geol. Soc. Lond. Spec. Publ.* 145, 73–90.
- Kendrick, J.E., Lavalée, Y., Varley, N.R., B, W.F., Lamb, O.D., Vasseur, J., 2016. Blowing off steam: tuffsite formation as a regulator for lava dome eruptions. *Front. Earth Sci.* 4, 41.
- Kennedy, B.M., Wadsworth, F.B., Vasseur, J., Schipper, C.I., Jelinek, A.M., von Aulock, F.W., Hess, K.-U., Russell, J.K., Lavallée, Y., Nichols, A.R., et al. 2016. Surface tension driven processes densify and retain permeability in magma and lava. *Earth Planet. Sci. Lett.* 433, 116–124.
- Klug, C., Cashman, K.V., 1996. Permeability development in vesiculating magmas: implications for fragmentation. *Bull. Volcanol.* 58, 87–100.
- Kolzenburg, S., Heap, M., Lavallée, Y., Russell, J., Meredith, P., Dingwell, D.B., 2012. Strength and permeability recovery of tuffsite-bearing andesite. *Solid Earth* 3, 191.
- Kushnir, A.R., Martel, C., Bourdier, J.-L., Heap, M.J., Reuschl, T., Erdmann, S., Komorowski, J.-C., Cholik, N., 2016. Probing permeability and microstructure: unravelling the role of a low-permeability dome on the explosivity of Merapi (Indonesia). *J. Volcanol. Geotherm. Res.* 316, 56–71.
- Kushnir, A.R., Martel, C., Champallier, R., Arbaret, L., 2017. In situ confirmation of permeability development in shearing bubble-bearing melts and implications for volcanic outgassing. *Earth Planet. Sci. Lett.* 458, 315–326.
- Liu, Y., Zhang, Y., Behrens, H., 2005. Solubility of H₂O in rhyolitic melts at low pressures and a new empirical model for mixed H₂O–CO₂ solubility in rhyolitic melts. *J. Volcanol. Geotherm. Res.* 143, 219–235.
- Maron, S.H., Pierce, P.E., 1956. Application of ree-yring generalized flow theory to suspensions of spherical particles. *J. Colloid Sci.* 11, 80–95.
- McGowan, E., 2016. Magma Emplacement and Deformation in Rhyolitic Dykes: Insight Into Magmatic Outgassing. Lancaster University. Ph.D. thesis.
- McKenzie, D., 1984. The generation and compaction of partially molten rock. *J. Petrol.* 25, 713–765.
- McKenzie, D., 2011. Compaction and crystallization in magma chambers: towards a model of the Skaergaard intrusion. *J. Petrol.* 52, 905–930.
- Melnik, O., Barmin, A., Sparks, R., 2005. Dynamics of magma flow inside volcanic conduits with bubble overpressure buildup and gas loss through permeable magma. *J. Volcanol. Geotherm. Res.* 143, 53–68.
- Miller, T.F., 1990. A numerical model of volatile behavior in nonwelded cooling pyroclastic deposits. *J. Geophys. Res. Solid Earth* 95, 19349–19364.
- Mueller, S., Llewellyn, E., Mader, H., 2010. The rheology of suspensions of solid particles. *Proc. Roy. Soc. Lond. A* 466, 1201–1228.
- Mueller, S., Llewellyn, E., Mader, H., 2011. The effect of particle shape on suspension viscosity and implications for magmatic flows. *Geophys. Res. Lett.* 38.
- Mueller, S., Melnik, O., Spieler, O., Scheu, B., Dingwell, D.B., 2005. Permeability and degassing of dome lavas undergoing rapid decompression: an experimental determination. *Bull. Volcanol.* 67, 526–538.
- Mueller, S.B., Ayris, P.M., Wadsworth, F.B., Kueppers, U., Casas, A.S., Delmelle, P., Taddeucci, J., Jacob, M., Dingwell, D.B., 2017. Ash aggregation enhanced by deposition and redistribution of salt on the surface of volcanic ash in eruption plumes. *Sci. Rep.* 7.
- Müller, R., Eberstein, M., Reinsch, S., Schiller, W., Deubener, J., Thiel, A., 2007. Effect of rigid inclusions on sintering of low temperature co-fired ceramics. *Phys. Chem. Glasses: Eur. J. Glass Sci. Technol., Part B* 48.
- Nakada, S., Shimizu, H., Ohta, K., 1999. Overview of the 1990–1995 eruption at Unzen Volcano. *J. Volcanol. Geotherm. Res.* 89, 1–22.
- Nakada, S., Uto, K., Sakuma, S., Eichelberger, J.C., Shimizu, H., 2005. Scientific results of conduit drilling in the Unzen scientific drilling project (USDP). *Sci. Drill.* 1, 18–22.
- Nara, Y., Meredith, P.G., Yoneda, T., Kaneko, K., 2011. Influence of macro-fractures and micro-fractures on permeability and elastic wave velocities in basalt at elevated pressure. *Tectonophysics* 503, 52–59.
- Neuberg, J.W., Tuffen, H., Collier, L., Green, D., Powell, T., Dingwell, D., 2006. The trigger mechanism of low-frequency earthquakes on Montserrat. *J. Volcanol. Geotherm. Res.* 153, 37–50.
- Nguyen, C.T., Gonnermann, H.M., Houghton, B.F., 2014. Explosive to effusive transition during the largest volcanic eruption of the 20th century (Novarupta 1912, Alaska). *Geology* 42, 703–706.
- Ni, H., Zhang, Y., 2008. H₂O diffusion models in rhyolitic melt with new high pressure data. *Chem. Geol.* 250, 68–78.
- Noguchi, S., Toramaru, A., Nakada, S., 2008. Groundmass crystallization in dacite dykes taken in Unzen scientific drilling project (USDP-4). *J. Volcanol. Geotherm. Res.* 175, 71–81.
- Okumura, S., Nakashima, S., 2004. Water diffusivity in rhyolitic glasses as determined by in situ IR spectroscopy. *Phys. Chem. Miner.* 31, 183–189.
- Okumura, S., Sasaki, O., 2014. Permeability reduction of fractured rhyolite in volcanic conduits and its control on eruption cyclicality. *Geology* 42, 843–846.
- Papale, P., 1999. Strain-induced magma fragmentation in explosive eruptions. *Nature* 397, 425–428.
- Quane, S.L., Russell, J.K., 2005. Welding: insights from high-temperature analogue experiments. *J. Volcanol. Geotherm. Res.* 142, 67–87.
- Quane, S.L., Russell, J.K., Friedlander, E.A., 2009. Time scales of compaction in volcanic systems. *Geology* 37, 471–474.
- Reubi, O., Blundy, J., Varley, N.R., 2013. Volatiles contents, degassing and crystallisation of intermediate magmas at Volcan de Colima, Mexico, inferred from melt inclusions. *Contrib. Mineral. Petrol.* 165, 1087–1106.
- Russell, J.K., Quane, S.L., 2005. Rheology of welding: inversion of field constraints. *J. Volcanol. Geotherm. Res.* 142, 173–191.
- Rust, A., Cashman, K., Wallace, P., 2004. Magma degassing buffered by vapor flow through brecciated conduit margins. *Geology* 32, 349–352.
- Saubin, E., Tuffen, H., Gurioli, L., Owen, J., Castro, J.M., Berlo, K., McGowan, E.M., Schipper, C.I., Wehbe, K., 2016. Conduit dynamics in transitional rhyolitic activity recorded by tuffsite vein textures from the 2008–2009 Chaitén eruption. *Front. Earth Sci.* 4, 59.
- Schipper, C.I., Castro, J.M., Tuffen, H., James, M.R., How, P., 2013. Shallow vent architecture during hybrid explosive–effusive activity at Cordón Caulle (Chile, 2011–12): evidence from direct observations and pyroclast textures. *J. Volcanol. Geotherm. Res.* 262, 25–37.
- Sparks, R., Tait, S., Yanev, Y., 1999. Dense welding caused by volatile resorption. *J. Geol. Soc.* 156, 217–225.
- Spieler, O., Kennedy, B., Kueppers, U., Dingwell, D.B., Scheu, B., Taddeucci, J., 2004. The fragmentation threshold of pyroclastic rocks. *Earth Planet. Sci. Lett.* 226, 139–148.
- Stasiuk, M.V., Barclay, J., Carroll, M.R., Jaupart, C., Ratté, J.C., Sparks, R.S.J., Tait, S.R., 1996. Degassing during magma ascent in the Mule Creek Vent (USA). *Bull. Volcanol.* 58, 117–130.
- Stewart, M.L., 2002. Dacite Block and Ash Avalanche Hazards in Mountainous Terrain: 2360 yr. BP Eruption of Mount Maeger, British Columbia. University of British Columbia. Ph.D. thesis.
- Thomas, M.E., Neuberg, J., 2012. What makes a volcano tick—first explanation of deep multiple seismic sources in ascending magma. *Geology* 40, 351–354.
- Tuffen, H., Dingwell, D., 2005. Fault textures in volcanic conduits: evidence for seismic trigger mechanisms during silicic eruptions. *Bull. Volcanol.* 67, 370–387.
- Tuffen, H., Dingwell, D.B., Pinkerton, H., 2003. Repeated fracture and healing of silicic magma generate flow banding and earthquakes? *Geology* 31, 1089–1092.
- Tuffen, H., Gilbert, J., McGarvie, D., 2001. Products of an effusive subglacial rhyolite eruption: Bláhnúkur, Torfajökull, Iceland. *Bull. Volcanol.* 63, 179–190.
- Wadsworth, F.B., Vasseur, J., Aulock, F.W., Hess, K.-U., Scheu, B., Lavallée, Y., Dingwell, D.B., 2014. Nonisothermal viscous sintering of volcanic ash. *J. Geophys. Res. Solid Earth* 119, 8792–8804.
- Wadsworth, F.B., Vasseur, J., Llewellyn, E.W., Schaubroth, J., Dobson, K.J., Scheu, B., Dingwell, D.B., 2016a. Sintering of viscous droplets under surface tension. *Proc. Roy. Soc. Lond. A* 472, 20150780.
- Wadsworth, F.B., Vasseur, J., Scheu, B., Kendrick, J.E., Lavallée, Y., Dingwell, D.B., 2016b. Universal scaling of fluid permeability during volcanic welding and sediment diagenesis. *Geology* 44, 219–222.
- Wagner, W., Cooper, J.R., Dittman, A., Kijima, J., Kretzschmar, H.-J., Kruse, A., Marès, R., Oguchi, K., Sato, H., Stöcker, I., Sifner, O., Y, T., Tanishita, I., Trübenbach, J., Willkommen, T., 2000. Iapws industrial formulation 1997 for the thermodynamic properties of water and steam. *Trans. AMSE* 122, 150–182.
- Wilson, C., 1984. The role of fluidization in the emplacement of pyroclastic flows, 2: experimental results and their interpretation. *J. Volcanol. Geotherm. Res.* 20, 55–84.
- Witham, C.S., Oppenheimer, C., Horwell, C.J., 2005. Volcanic ash-leachates: a review and recommendations for sampling methods. *J. Volcanol. Geotherm. Res.* 141, 299–326.
- Woods, A.W., Koyaguchi, T., 1994. And effusive eruptions of silicic magmas. *Nature* 370, 25.
- Zhang, Y., 1999. H₂O in rhyolitic glasses and melts: measurement, speciation, solubility, and diffusion. *Rev. Geophys.* 37, 493–516.
- Zhang, Y., Behrens, H., 2000. H₂O diffusion in rhyolitic melts and glasses. *Chem. Geol.* 169, 243–262.
- Zhang, Y., Ni, H., 2010. Diffusion of H, C, and O components in silicate melts. *Rev. Mineral. Geochem.* 72, 171–225.
- Zhang, Y., Stolper, E.M., Wasserburg, G., 1991. Diffusion of water in rhyolitic glasses. *Geochim. Cosmochim. Acta* 55, 441–456.